Thermal evolution of the North Atlantic lithosphere: New constraints from magnetic anomaly inversion with a fractal magnetization model

Chun-Feng Li and Jian Wang

State Key Laboratory of Marine Geology, Tongji University, Shanghai 200092, China (cfl@tongji.edu.cn)

Jian Lin

Department of Geology and Geophysics, Woods Hole Oceanographic Institution, Woods Hole, Massachusetts, USA

Tingting Wang

State Key Laboratory of Marine Geology, Tongji University, Shanghai, China

[1] Using recently published global magnetic models, we present the first independent constraint on North Atlantic geothermal state and mantle dynamics from magnetic anomaly inversion with a fractal magnetization model. Two theoretical models of radial amplitude spectrum of magnetic anomalies are found almost identical, and both are applicable to detecting Curie depths in using the centroid method based on spectral linearization at certain wave number bands. Theoretical and numerical studies confirm the robustness of this inversion scheme. A fractal exponent of 3.0 in the magnetic susceptibility is found suitable, and Curie depths are well constrained by their known depths near the mid-Atlantic ridge. While generally increasing with growing ages, North Atlantic Curie depths show large oscillating and heterogeneous patterns related most likely to small-scale sublithospheric convections, which are found to have an onset time around 40 Ma and a scale of about 500 km, and are in preferred transverse rolls. Hotspots in North Atlantic also contribute to large geothermal and Curie-depth variations, but they appear to connect more closely to geochemical anomalies or small-scale convection than to mantle plumes. Curie depths can be correlated to heat flow gridded in a constant 1° interval, which reveals decreasing effective thermal conductivity with depths within the magnetic layer. North Atlantic Curie points are mostly beneath the Moho, suggesting that the uppermost mantle is magnetized from serpentinization and induces long-wavelength magnetic anomalies. Small-scale convection and serpentinization together may cause apparent flattening and deviations in heat flow and bathymetry from theoretical cooling models in old oceanic lithosphere.

1. Introduction

[2] North Atlantic and its two conjugate continental margins are the primary places where we obtain our knowledge of continental rifting and seafloor spreading. The Atlantic is also an ideal place for studying near-ridge and intraplate hotspots, e.g., Iceland, Azores, Bermuda Rise (BR), Canary Islands (CI), and Cape Verde Islands (CVI), and how they interplay with ridges, transform faults, fractures, and the oceanic lithosphere (Figure 1a). Thermal state of the Atlantic lithosphere is a critical piece of information in better understanding these geological processes.

[3] Our abilities in detecting thermal state of oceanic lithosphere are limited to either numerical modeling or surface-heat-flow measurements. Numerical modeling is basically a forward process, assuming certain types of thermal parameters and boundary conditions [*Parker and Oldenburg*, 1973; *Parsons and Sclater*, 1977; *Fleitout and Yuen*, 1984; *Doin and Fleitout*, 1996]. If a good match between the model and the observation is made, the model and its parameters are considered being viable. In this case, often only idealized geometries are taken. Surface-heat-flow measurements suffer from being only available at sparse and irregular locations and are relatively insensitive to deep temperature variations due to a long delay between a change in asthenosphere temperature and a measurable effect arriving at the surface [*Korenaga*, 2009; *Foulger*, 2012]. Therefore, surface heat flow alone is not sufficient in inferring deep lithospheric temperature. Shear wave velocity from seismic tomography can also give clues to lithospheric temperature anomalies, but large-scale high-resolution seismic tomographies of oceanic lithosphere are very rare. Due to these limitations, there still remain many unanswered questions on the cooling process of oceanic lithosphere and sublithosphere convective patterns [e.g., *Korenaga and Korenaga*, 2008; *Adam and Vidal*, 2010].

[4] While magnetic anomalies contributed greatly to the early development of plate tectonics, they have not been widely applied to infer oceanic lithospheric structures, due to limited data coverage and data processing difficulties. Over the last several years, global compilations of magnetic anomalies become available at increasing resolutions (Figure 1b) [*Hamoudi et al.*, 2007; *Hemant et al.*, 2007; *Purucker*, 2007; *Maus et al.*, 2009]. These valuable data assets, strengthened with improved data processing algorithms, open a new way of investigating large-scale lithospheric magnetization and geothermal state [e.g., *Purucker and Whaler*, 2007; *Bouligand et al.*, 2009; *Li et al.*, 2010, 2012; *Li*, 2011; *Purucker and Clark*, 2011]. Being a good proxy to subsurface temperature variation, the mapped depth to the Curie-point temperature puts an observable and direct constraint on the 3-D geothermal structure of the Atlantic lithosphere, which cannot be easily assessed otherwise. Thus, difficulties in inferring subsurface temperatures using surface heat flow can be partially circumvented by directly locating Curie-point depths.

[5] This study is based mainly on the Earth Magnetic Anomaly Grid of 2 arc-minute resolution (EMAG2; Figure 1b) [*Maus et al.*, 2009], but an early grid for the World Digital Magnetic Anomaly Map of 3 arc-minute resolution (EMAG3) [*Maus et al.*, 2007] is also examined for double-checking our own algorithms and different interpolation effects in the original magnetic grids. Although inferring continental Curie depths from magnetic anomalies has been successfully carried out for some years, few studies have been published in oceanic regions, especially in places where active spreading process is ongoing. The presence of active spreading ridge of North Atlantic will provide an important benchmark for the inversion algorithm and estimated Curie depth, because near the ridge axis the active magmatism and high temperature will cause the thickness of the magnetic layer to be virtually zero. As a result, the depth to the magnetic top at one particular position will be nearly equal to the depth to the magnetic bottom, and both should be close to the bathymetric depth of the spreading axis.

[6] The framework of this paper is as follows. Theoretical models of radially averaged amplitude spectrum of magnetic anomalies are introduced, and their assumptions and applicability are
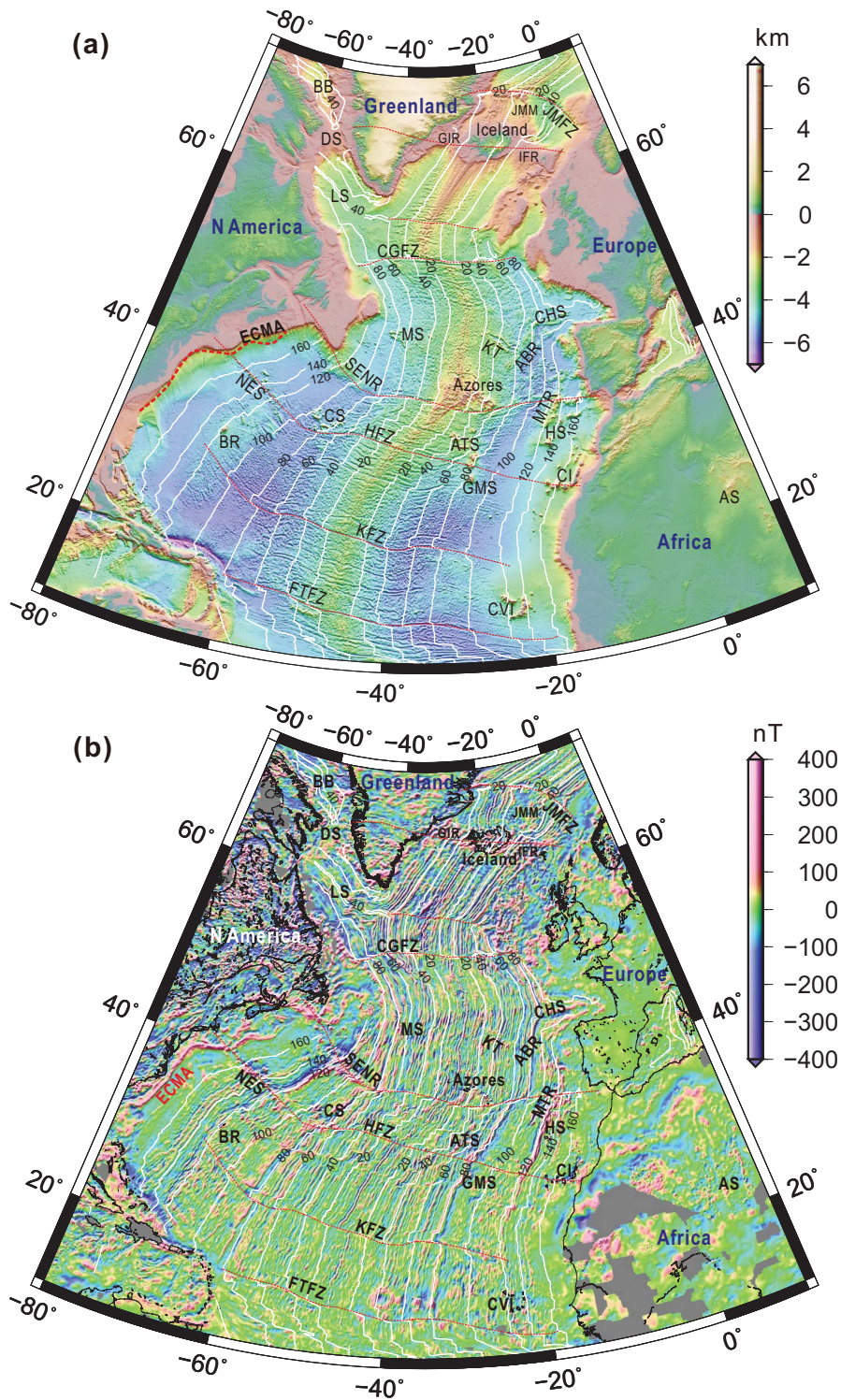
Figure 1. (a) North Atlantic bathymetry and topography (data from *Smith and Sandwell* [1997]). (b) North Atlantic magnetic anomalies based on EMAG2 [*Maus et al.*, 2009]. Maps are in Albers equal-area conic projection. Crustal isochrons are based on *Müller et al.* [2008]. Thin red dashed lines are fracture zones. The thick red dashed line labels the East Coast Magnetic Anomaly (ECMA). Features marked are Azores-Biscay Rise (ABR), Ahaggar Swell (AS), Atlantis seamounts (ATS), Baffin Bay (BB), Bermuda Rise (BR), Charlie Gibbs Fracture Zone (CGFZ), Charcot seamounts (CHS), Canary Islands (CI), Ceara Rise (CR), Corner seamounts (CS), Cape Verde Islands (CVI), Davis Strait (DS), Fifteen Twenty Fracture Zone (FTFZ), Great Meteor seamounts (GMS), Greenland-Iceland Ridge (GIR), Hayes Fracture Zone (HFZ), Horseshoe seamounts (HS), Iceland-Faeroe Ridge (IFR), Jan Mayen Fracture Zone (JMFZ), Jan Mayen microcontinent (JMM), Kane Fracture Zone (KFZ), Kings Trough (KT), Labrador Sea (LS), Milne seamounts (MS), Madeira Tore Rise (MTR), New England seamounts (NES), and Southeast Newfoundland Ridge (SENR).

discussed. This is followed by a numerical synthetic test of the computational algorithm by generating layered models of 3-D fractal magnetizations of known tops and bottoms, forward computing synthetic magnetic anomalies, and then inverting for Curie depths. Curie depths of the North Atlantic are then calculated with moving windows of various sizes. With a joint analysis of Curie depths and surface heat flow, geothermal structure and evolution of the Atlantic lithosphere are studied, with inferences to upper mantle magnetization, small-scale convection, and geothermal anomalies of hotspots.

2. Theoretical Models of Radial Amplitude Spectrum of Magnetic Anomalies

[7] Almost all natural geophysical properties are spatially correlated and thus scaling laws are required to describe them. A 3-D fractal magnetization model has a power spectrum of magnetization proportional to the norm of the wave number raised to power $-\beta_{3D}^{p}$:

$$\phi_M(k_x, k_y, k_z) \propto k^{-\beta_{3D}^{p}},$$

in which $\phi_M(k_x, k_y, k_z)$ is the 3-D power spectrum of the magnetization, k_x, k_y, and k_z are wave numbers in x, y, and z directions, respectively, and their Euclidean norm $k = \sqrt{k_x^2 + k_y^2 + k_z^2}$. Following *Maus et al.* [1997] and *Bouligand et al.* [2009], the analytic expression for the 1-D radial amplitude spectrum of the 2-D magnetic anomalies from the 3-D fractal magnetization model can be written as

$$\ln\left[A_{\Delta T}^{M}(k, Z_t, Z_b, \beta_{3D}^{p})\right] = C1 - |2\pi k|Z_t$$
$$- \frac{\beta_{3D}^{p}-1}{2}\ln|2\pi k| - |\pi k|(Z_b - Z_t)$$
$$+ \frac{1}{2}\ln\left\{\frac{\sqrt{\pi}}{\Gamma\left(1+\frac{\beta_{3D}^{p}}{2}\right)}\left[\frac{\text{Cosh}\left(|2\pi k|(Z_b - Z_t)\right)}{2}\Gamma\left(\frac{1+\beta_{3D}^{p}}{2}\right)\right]\right.$$
$$\left. - K_{(1+\beta_{3D}^{p})/2}(|2\pi k|(Z_b - Z_t))(|\pi k|(Z_b - Z_t))^{(1+\beta_{3D}^{p})/2}\right\}, \tag{1}$$

where Γ is the gamma function, K is the modified Bessel function of the second kind, $A_{\Delta T}^{M}$ is the radially averaged amplitude spectrum of total field magnetic anomalies, with the superscript M indicating the definition by *Maus et al.* [1997], k is the wave number, C1 is a constant related to magnet-

ization direction and geomagnetic field direction, and Z_b and Z_t are depths to the bottom and top of the magnetic layer, respectively. Depths to the bottom of magnetic sources are regarded as the Curie-point depth, where minerals reach their Curie temperatures and lose their ferromagnetism.

[8] Alternatively, for a model with 2-D horizontal fractal magnetization but a constant vertical magnetization, the 1-D radial amplitude spectrum can be written as [*Blakely*, 1995; *Li et al.*, 2009]

$$\ln\left[A_{\Delta T}^{B}(k, Z_t, Z_b, \beta_{3D}^{p})\right]$$
$$= C2 - |2\pi k|Z_t - \frac{\beta_{3D}^{p}-1}{2}\ln|2\pi k| + \ln\left[1 - e^{-|2\pi k|(Z_b - Z_t)}\right], \tag{2}$$

with the assumptions of infinite horizontal extensions of magnetic sources and much smaller depths than horizontal scales. Here $A_{\Delta T}^{B}$ is the radially averaged amplitude spectrum of the total field magnetic anomalies, with the superscript B indicating the definition by *Blakely* [1995], C2 is a constant related to magnetization direction and geomagnetic field direction, and $k = \sqrt{k_x^2 + k_y^2}$. Note here that β_{3D}^{p} is defined in the power spectrum of the 3-D magnetization, and it has been shown that β_{3D}^{p} is nearly larger by 1 than that of a model with a 2-D horizontal fractal magnetization but a constant vertical magnetization [*Maus and Dimri*, 1994; *Maus et al.*, 1997; *Bouligand et al.*, 2009]. Thus, $\beta_{3D}^{p} - 1 \approx \beta_{2D}^{p}$.

[9] Although the Maus model (equation (1)) takes a rather complicated form from the solution of an integral by *Bouligand et al.* [2009], it can be realized from equations (1) and (2) that both models have some common terms. Indeed, it can be shown mathematically that for sufficiently large k, the sum of the last two terms in equation (1) approaches a constant related only to the fractal exponent β_{3D}^{p}, and the last term in equation (2) will asymptotically become zero. Therefore, both models can be approximated to

$$\ln\left[A_{\Delta T}(k, Z_t, \beta_{3D}^{p})\right] \approx C - |2\pi k|Z_t - \frac{\beta_{3D}^{p}-1}{2}\ln|2\pi k|, \tag{3}$$

where C is a constant. Equation (3) forms the linear basis of estimating Z_t at intermediate to high wave number band.

[10] Next we visually examine the difference and similarity of these two models by plotting them against each other (Figure 2a). For both models, the input β_{3D}^{p} is 3, and Z_b and Z_t are 20 and 2 km, respectively. One can see that these two models
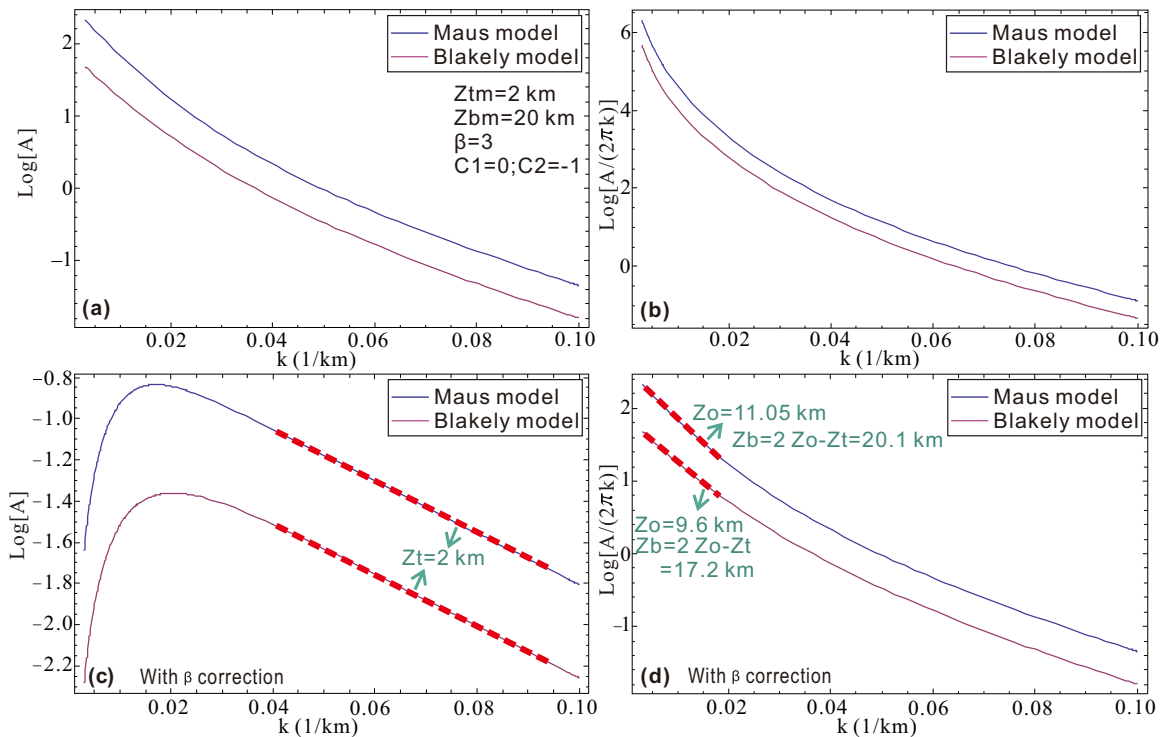
Figure 2. Comparison between the two theoretical models (equations (1) and (2)) of radially averaged amplitude spectra of magnetic anomalies. (a) Theoretical models with input depths to the top (Z_{tm}) and bottom (Z_{bm}) of the magnetic layer of 2 and 20 km, respectively. (b) Wave-number-scaled theoretical models (radial amplitude spectra). (c) Radial amplitude spectra in Figure 2a after the fractal exponent correction. (d) Wave-number-scaled radial amplitude spectra in Figure 2b after the fractal exponent correction. Red dashed line segments show the wave number bands where depths to the top and centroid of the magnetic layer are estimated using equations (3) and (4).

are nearly identical in shapes except for a vertical constant shift. After corrections for β_{3D}^p, which amounts to add the last term of equation (3) to the spectra, both models can give faithful estimates of Z_t from simple linear regressions at intermediate to high wave number bands (Figure 2c). At small wave number band, *Tanaka et al.* [1999] approximated the Blakely model (equation (2)) by a linear formula of the depth to the centroid Z_0 of the magnetic layer:

$$\ln\left[\frac{A_{\Delta T}\left(k, Z_0, \beta_{3D}^p\right)}{|2\pi k|}\right] \approx C3 - |2\pi k| Z_0 - \frac{\beta_{3D}^p - 1}{2}\ln|2\pi k|, \quad (4)$$

where C3 is a constant. The close similarity between the two models (Figure 2b), therefore, indicates that the same linear approximation can be applied with the Maus model in estimating Z_0. The centroid is the midpoint between the top and bottom of the magnetic source. After corrections for β_{3D}^p, the Maus model gives an Z_b estimate of 20.1 km, while the Blakely model leads to an estimate of 17.2 km, and both estimates from linear

regressions using equation (4) are close to the input Z_b of the model.

[11] We further examine the behaviors of these two models and their linear approximations by testing with different Z_b (Figure 3). Again, we observe very similar patterns between the two models for different Z_b. Both models demonstrate that Z_b variations affect predominantly the small wave numbers of radial amplitude spectra, and increasing Z_b can only be differentiated at increasingly smaller and narrower wave number bands (Figures 3a1 and 3b1). Because of this, larger Z_b will be estimated with growing errors and decreasing resolutions. The estimations of Z_t are more robust, because all Z_b models except for the very shallow Z_b of 5 km converge well at the intermediate to high wave number band (Figures 3a3 and 3b3). Very shallow Z_b will tend to bias the estimated Z_t.

[12] Figure 3 also demonstrates the importance of performing β_{3D}^p corrections before linear regressions for depths. Without corrections, estimated Z_b can be too large and at the same time at very low
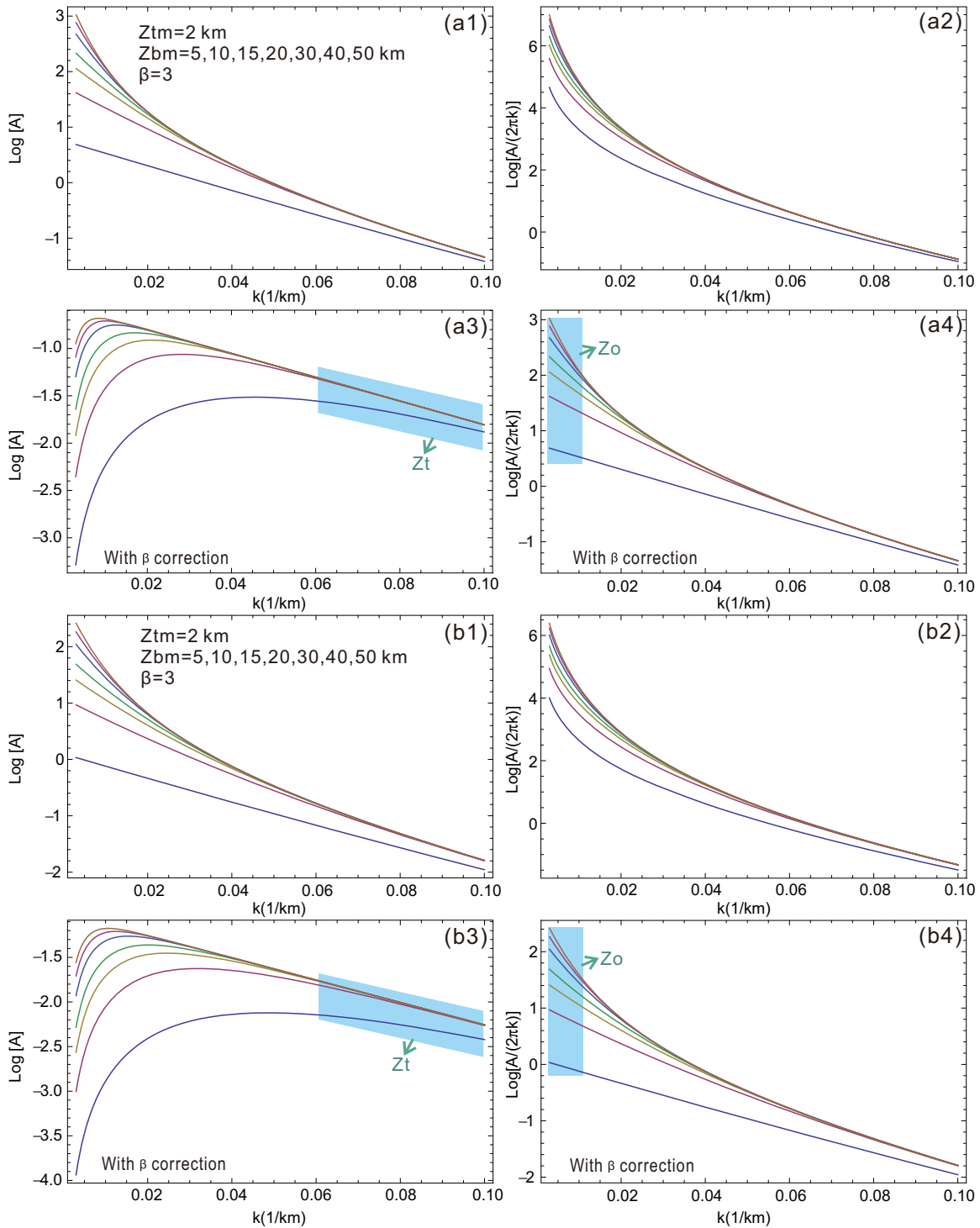
Figure 3. Comparison between the two theoretical models (equations (1) and (2)) of radially averaged amplitude spectra of magnetic anomalies for different Curie-depth models. Figures 3a1–3a4 are based on the Maus model (equation (1)), and Figures 3b1–3b4 are from the Blakely model (equation (2)). Z_{tm} and Z_{bm} are input depths to the top and bottom of the magnetic layer, respectively. Blue shadowed regions show the wave number bands where depths to the top and centroid of the magnetic layer are estimated using equations (3) and (4).

resolutions (Figures 3a2 and 3b2). β_{3D}^p correction removes the effect of potentially shallow but spatially correlated magnetizations with long wavelengths and will make the radial amplitude spectra of different Z_b more differentiable at small wave numbers (Figures 3a4 and 3b4). Because our input $\beta_{3D}^p = 3$, it just happens that the β_{3D}^p-corrected and wave number-scaled amplitude spectra (Figures 3a4 and 3b4) will be identical to the original amplitude spectra defined by equations (1) and (2) (Figures 3a1 and 3b1). This is just a coincidence and the same identity will not hold for other fractal exponents.

[13] Given the close similarity between the two mathematical models, in subsequent applications, we apply linear approximations based on the Blakely model only, since this model is almost equivalent to the Maus model but enjoys a simpler mathematical treatment. It is interesting to note that *Maus et al.* [1997] applied radial average of the logarithm of the amplitude spectrum in deriving equation (1), whereas *Blakely* [1995] defined equation (2) using the logarithm of radial average of the amplitude spectrum. However, since these two equations are nearly identical from above discussions, the order of mathematical operations should not concern us. Certainly, the numerical values for a specific wave number from these two different orders of operations will differ, but their overall shapes, from which our depths are estimated, are the same. To see this point, we notice, from both *Maus et al.* [1997] and *Blakely* [1995], that the amplitude spectrum can be factorized into an azimuthal term and a second term independent of azimuth θ. Therefore, the logarithm of the radial average of the amplitude spectrum is

$$\ln\left[\frac{1}{2\pi}\int_0^{2\pi} A_{\Delta T}(\theta, k)d\theta\right] = \ln\left[\frac{1}{2\pi}\int_0^{2\pi} f(\theta)f(k)d\theta\right]$$
$$= \ln[f(k)] + \ln\left[\frac{\int_0^{2\pi} f(\theta)d\theta}{2\pi}\right], \quad (5)$$

and the radial average of the logarithm of the amplitude spectrum is

$$\frac{1}{2\pi}\int_0^{2\pi}\ln[A_{\Delta T}(\theta, k)]d\theta = \frac{1}{2\pi}\int_0^{2\pi}\ln[f(\theta)f(k)]d\theta = \ln[f(k)]$$
$$+ \frac{1}{2\pi}\int_0^{2\pi}\ln[f(\theta)]d\theta. \quad (6)$$

[14] Note that the last terms in both equations (5) and (6) are constants, and the two different mathe-

matical orders differ only by a constant, thereby having no effects theoretically on Z_b estimations. Our calculation is based on the logarithm of the radial average of the amplitude spectrum, conformable to equation (2) of the Blakely model. Although *Maus and Dimri* [1995] and *Maus et al.* [1997] argued that the radial average of the logarithm of the amplitude spectrum is preferred, this is not required computationally. Even the synthetic test of *Maus and Dimri* [1995] shows that the two mathematical procedures give essentially the same result in the long-wavelength (small wave number) domain ($k < 0.1$ km^{-1}), within which our Z_b is estimated.

[15] It is confirmed theoretically that this Curie-depth inversion scheme does not require whether the source magnetizations are induced or remanent and therefore does not require reduction to the pole [*Okubo et al.*, 1985; *Blakely*, 1995; *Maus et al.*, 1997]. This is advantageous for studying oceanic lithospheres where strong remanent magnetizations are known to exist. First, the two models consider frequency spectra of magnetic ensembles within a window rather than of individual magnetic bodies. Whether magnetizations of parts or all magnetic sources are reduced or remanent is expected to have little effects on the ensemble spectrum. Second, reduction to the pole is a phase operation only and theoretically has no effects on wave numbers and thereby on estimated Z_b, though a small spatial shift in Z_b is possible with reduction to the pole [*Li*, 2011].

[16] Although marine magnetic anomalies are characterized by lineations that could cause anisotropic fractal exponents, it was found in the South China Sea that normalized autocorrelation functions of typical marine magnetic anomalies have near-circular autocorrelation coefficients, indicating no strong trends in the data that could modify the slopes of radially averaged spectra [*Li et al.*, 2010]. Both the 3-D Maus model and the 2-D Blakely model remove directional effects of magnetization and geomagnetic field in their derivations by getting 1-D radially averaged amplitude spectra, and the anisotropy of the field is reflected only in the constant term [*Maus and Dimri*, 1995; *Maus et al.*, 1997]. Therefore, these two models are appropriate for the oceanic context. It is unlikely that magnetization in oceanic crust is scaled only in one dimension, because all processes, like spreading rate, thickness of magnetic layer, Earth's magnetic field, and rock chemistry and susceptibility, are all variable and can produce 2-D and 3-D scaling of magnetization. One

alternative approach would be to use individual profiles or cross sections perpendicular to the lineation direction to estimate the depths [*Hassanzadeh*, 1976; *Blakely and Hassanzadeh*, 1981], but magnetic anomalies along a profile bear contributions from adjacent magnetic sources not directly beneath the profile. Therefore, this profile approach has no advantage over the windowed technique applied in this paper.

3. Numerical Synthetic Test of the Methodology

[17] The theoretical models and the linearized inversion scheme are further tested here with numerical synthetic models. Here we apply a modeling approach very similar to that used in *Pilkington and Todoeschuck* [1993] and *Bouligand et al.* [2009]. To generate the 3-D fractal magnetization model, we first produce a 3-D random matrix of $500 \times 500 \times 500$ cells according to the Gaussian distribution. The 3-D Fourier transform of this random matrix, with zero-frequency component shifted to the center, is then modulated by the Euclidean norm of the wave number to a power of $-\beta_{3D}^p/2$. In this case, we choose $\beta_{3D}^p=3$. The modulated 3-D Fourier transform is then transformed back to the space domain and converted to have a zero mean and a standard deviation of 0.3 A/m. A subspace of this fractal model is shown in Figure 4a.

[18] We then calculate the magnetic anomalies directly above magnetic models of various thicknesses extracted from the 3-D fractal magnetization model (Figure 4). This is achieved by calculating the 2-D Fourier transforms of magnetizations of each single layer of cells within the model, multiplying the transforms with the Earth filter [*Blakely*, 1995], summing up the results together, and finally computing the inverse transform. For different models, we keep their tops and overlapping volumes to be the same and extend their bottoms only. For computing simplicity but without losing generality, we assume that the magnetizations and observations are obtained at the North Pole. Our algorithm, however, can compute magnetic anomalies of 3-D fractal magnetization volumes at any directions of magnetization and of geomagnetic field.

[19] Figure 4 shows four subsets of magnetic anomalies directly above the subspace of the fractal model shown in Figure 4a. It is seen that with increasing thicknesses, long-wavelength components increase in the calculated anomalies, though the overall features remain similar. The largest difference in anomalies occurs between models with small input Curie depths (Z_{bm}) of 10 and 20 km. This confirms that increasing Z_b can only be differentiated at increasingly smaller and narrower wave number bands, as already demonstrated by the theoretical models (Figures 3a1 and 3b1).
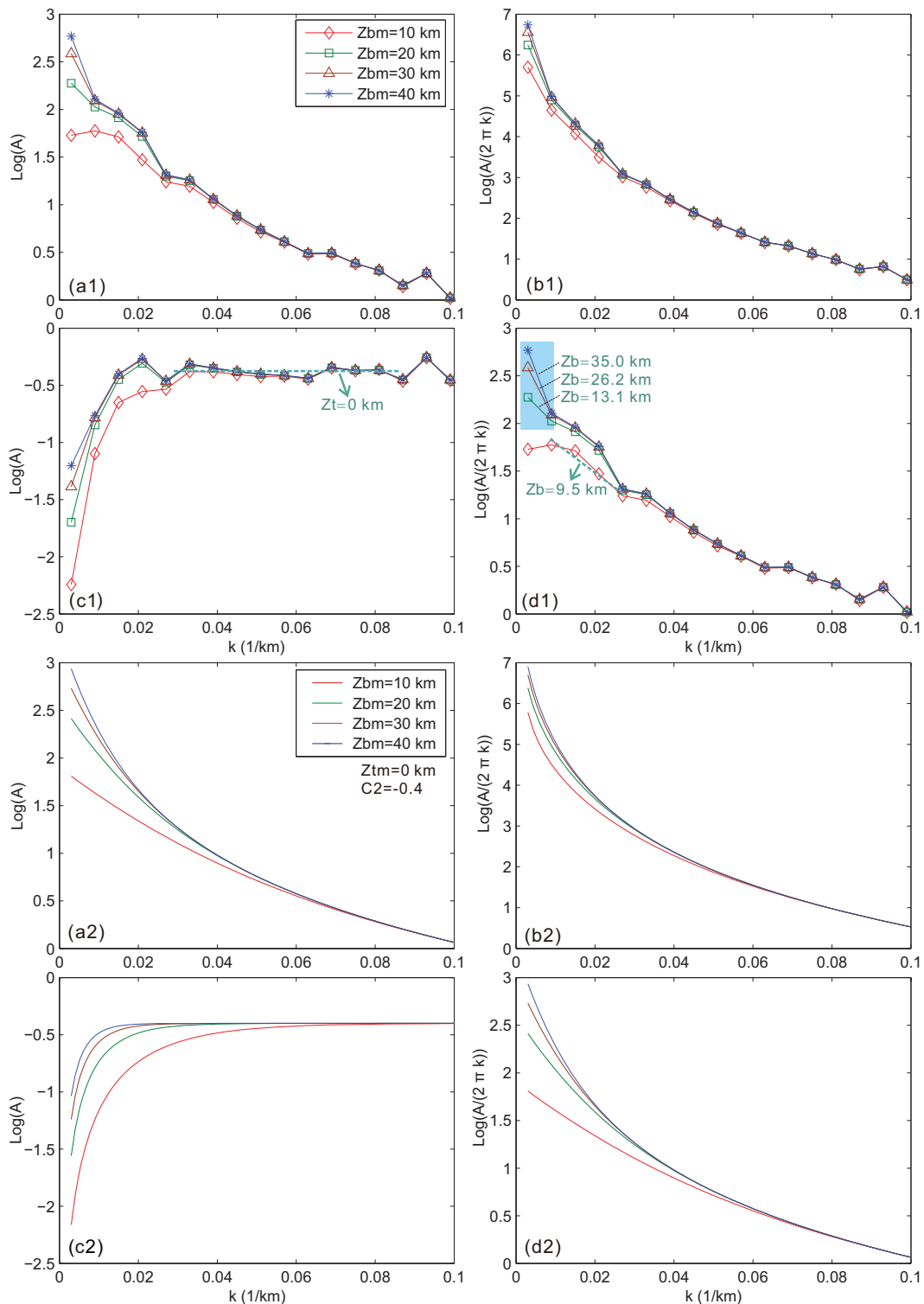
[20] Figure 5 plots radially averaged spectra of simulated magnetic anomalies, which are very similar to theoretical predictions seen from Figure 3. Again, it is observed that spectra from models of different Z_b are only differentiable at small wave numbers. Figure 5c1 shows that all four radially averaged spectra after the fractal exponent correction converge at middle to large wave numbers, and their linear regressions give an estimated top depth of 0 km based on equation (3). This inverted depth equals exactly the input depth to the top of the synthetic models. Based on the β_{3D}^p-corrected and wave-number-scaled amplitude spectra (Figure 5d1), and from linear regressions at small wave number band using equation (4), we find that the estimated Z_b is close to, but slightly smaller than, the Z_b of the models.

[21] Theoretical models shown in Figures 3 and 5 do not have spectral peaks even for very small Z_b, if the fractal exponent is equal to 3. But in the numerical synthetic test with the same fractal exponent, there is a spectral peak when Z_b of the model equals 10 km. This peak is caused by the finite size of the numerical model that causes preferential drops in long-wavelength components, while the theoretical models are infinite in horizontal extensions. This also explains why the estimated Z_b is slightly but consistently smaller than the Z_b of input models. Using more data points in numerical models is possible, though the results will be slightly underestimated. Even so, we can use four data points (broader regression interval) for regression in the numerical synthetic model when input Curie depth $Z_{bm} = 10$ km because in this case the target depth to be estimated is shallow. For either the theoretical data or the real data, underestimation is less problematic so we can apply broader wave number ranges in linear regressions. For real data, underestimation can also be overcome with slightly smaller corrections for the fractal exponent β_{3D}^p. As expected, numerical computing introduces small undulations in the spectra, but we have demonstrated the close similarity between the numerical spectra and their theoretical counterparts (based on the Blakely model)
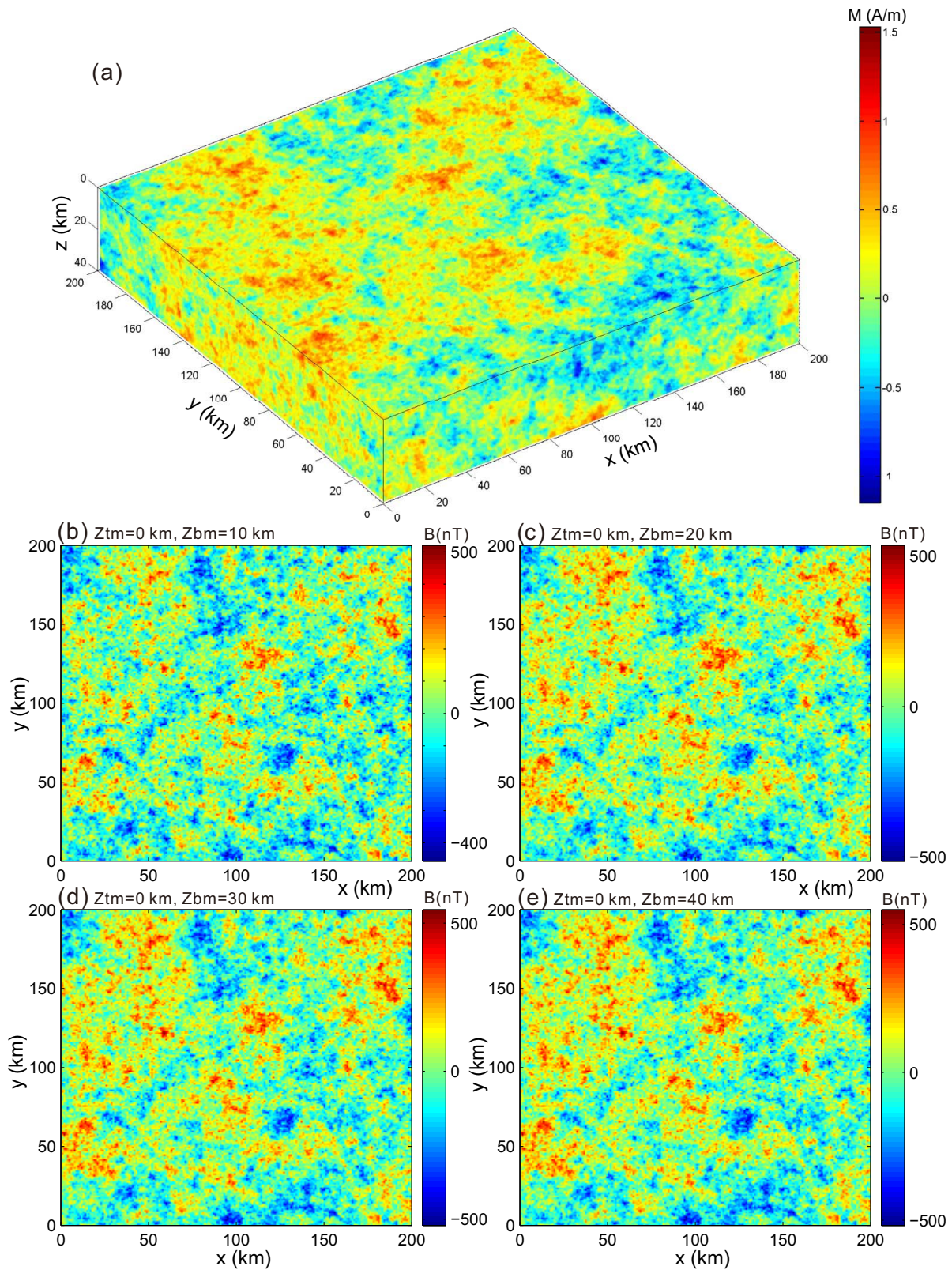
Figure 4. Synthetic numerical modeling of fractal magnetization models of various Curie depths and their magnetic anomalies. Fractal exponent β^p_{3D} of the input model is 3. (a) A subspace of the 3-D fractal magnetization model. (b)–(e) Calculated magnetic anomalies based on the 3-D fractal magnetization of Figure 4a with a fixed top (0 km in depth) but variable bottoms (Curie depths in 10, 20, 30, and 40 km, respectively).

Figure 5. (a1) Radially averaged amplitude spectra of the four sets of synthetic magnetic anomalies in Figure 4. (b1) Wave-number-scaled radial amplitude spectra. (c1) Radial amplitude spectra in Figure 5a1 after the fractal exponent correction. (d1) Wave-number-scaled radial amplitude spectra in Figure 5b1 after the fractal exponent correction. Figures 5a2, 5b2, 5c2, and 5d2 show the theoretical counterparts of Figures 5a1, 5b1, 5c1, and 5d1, respectively. These theoretical curves, based on the Blakely model, are drawn using the same parameters as those used in the numerical simulation. Window size = 200 km. Shallow blue dashed line segments and blue shadowed regions show the wave number bands where depths to the top and centroid of the magnetic layer are estimated using equations (3) and (4).

that are drawn using the same parameters as those used in the numerical simulation (Figures 5a2–5d2).

[22] It is noticed that when Z_b to be estimated is smaller, the linear regression wave number band can be broader and extend to slightly larger wave numbers. This is also expected and required by the theory (Figure 3) since smaller Z_b results in larger wave number components. From numerical differences between input and estimated depths of these synthetic tests, it is estimated that the largest error in estimated Z_b using the linearized centroid method employed in this paper will not reach 35%, provided that the selected fractal exponent and wave number bands for linear regressions are reasonable. In fitting the slopes of amplitude spectra, we use a least squares fitting method that automatically select the proper fitting interval for depth estimation in cases that the first or two data points of the smallest wave numbers in the amplitude spectra have smaller values than following points, as we did in Figure 5d2 in the case of a modeled Z_b of 10 km.

[23] Recently, *Bansal et al.* [2011] applied nearly the same method as the one shown here in estimating Curie depths. However, in their calculations they often estimate Z_t (depth to the magnetic top) in the very small wave number ranges, like the way we estimate Z_0. Therefore, their application of the methodology in estimating Z_t (and therefore, Z_b) is not theoretically based. In addition, their algorithm is not automated and incapable of computing densely gridded Curie depths for a very large area.

4. Magnetic Anomaly Models of North Atlantic

[24] Compiled from satellite, ship, and airborne magnetic measurements, the EMAG2 (http://geomag.org/; Figure 1b) [*Maus et al.*, 2009] is a significant update of a previous candidate grid for the World Digital Magnetic Anomaly Map (EMAG3, http://geomag.org/; Figure 6b) [*Maus et al.*, 2007]. In EMAG2, the altitude has been reduced from 5 to 4 km above the geoid, and additional grid and track line data have been included, both over land and the oceans.

[25] To improve the representation of the oceanic magnetic lineations, directional gridding by the least squares collocation using an anisotropic correlation function has been applied to extrapolate

the field into unsurveyed areas in EMAG2 [*Maus et al.*, 2009], based on the oceanic crustal age model by *Müller et al.* [2008]. This procedure significantly improves the visual appearance of EMAG2 but may lead to smoother than the true magnetic field [*Maus et al.*, 2009]. Because of this, the spectral content of the model could be changed from that of the underlying data, and this therefore could affect Z_b estimates. However, *Maus et al.* [2009] noted that the anisotropy of the true correlation function was maintained, and the anisotropy of the oceanic field in EMAG2 is realistic, even if the overall appearance is smoother than real.

[26] Furthermore, our study area, North Atlantic, is one of the best surveyed areas in the world. Figure 6a shows part of the survey tracks over North Atlantic in the candidate grid for the World Digital Magnetic Anomaly Map (EMAG3) [*Maus et al.*, 2007], upon which the new EMAG2 grid is further built. It is seen from Figure 6a that dense magnetic survey tracks cover most parts of the ocean, except in the southeastern corner of the study area (the Labrador Sea and Baffin Bay areas have other grids that are not shown). Therefore, the effects of directional gridding should be minimal. In our calculations, we have excluded areas constrained only by satellite data, and these areas have already been masked in the original magnetic maps (Figures 1b and 6b), as well as in maps of calculated Z_b derived from these two maps.

[27] The previous grid EMAG3 is a 3 arc-minute grid of the total intensity anomaly at 5 km above the World Geodetic System (WGS84) geoid (Figure 6b). No directional gridding was applied in producing EMAG3. In the next section we will further examine the effects of directional gridding and double-check our algorithms by comparing estimated Z_b from both EMAG2 and EMAG3.

5. Estimating Curie-Point Depths of North Atlantic

[28] The linearized equations (equations (3) and (4)) reduce four unknown parameters (Z_b, Z_t, β_{3D}^p, and a constant) in the original models (equations (1) and (2)) down to 3 (either Z_t, β_{3D}^p, and a constant, or Z_b, β_{3D}^p, and a constant). Even so, simultaneous nonlinear inversion for three unknowns is often difficult and unstable [*Ravat et al.*, 2007; *Li et al.*, 2009, 2010]. Very often a constant fractal exponent β_{3D}^p is assumed. The active North
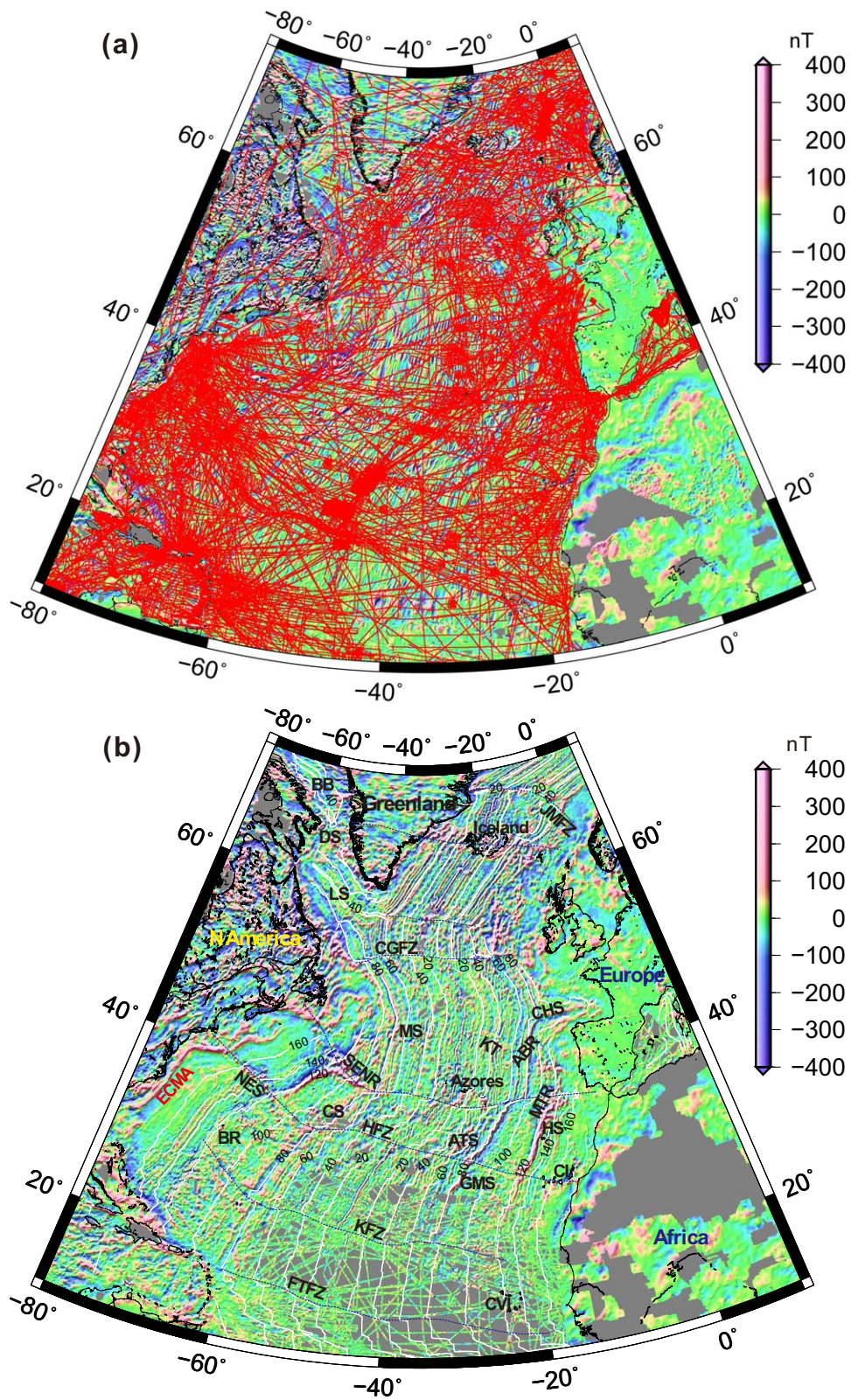
Figure 6. (a) Magnetic survey tracks of EMAG3 in North Atlantic. The background is North Atlantic magnetic anomalies from EMAG2. (b) North Atlantic magnetic anomalies from EMAG3.

Atlantic ridge, where the thermal and magnetic structures are well understood, serves as an excellent benchmark for choosing β_{3D}^p. The depths to the volcanic basement of North Atlantic should be close to Z_t, and at the active spreading center, both Z_b and Z_t should be numerically close to each other and approach the bathymetric depths of the spreading axis, as expected. This is indeed the case when $\beta_{3D}^p=3$ (Figure 7), and our selection of β_{3D}^p is well constrained at the active spreading center by the estimated Z_b and Z_t themselves. This value of β_{3D}^p is also close to other suggested values in continental areas [e.g., *Pilkington and Todoeschuck*, 1993, 1995; *Bouligand et al.*, 2009]. By choosing a larger or smaller β_{3D}^p, the estimated Z_b will slightly decrease or increase, respectively, but the overall Z_b pattern will not change on a map view. Once β_{3D}^p is assumed, we correct the calculated radial spectra by moving the last item involving β_{3D}^p in equations (3) and (4) to the left-hand side. The resulting spectra are then taken to be independent of β_{3D}^p.

[29] In computing radial amplitude spectra, we apply a constant wave number interval of 0.006 km^{-1}. The centroid depths (Z_o) are estimated primarily from the spectral wave number range of 0.003–0.03 km^{-1}, and the top depths to the magnetic sources are estimated within the wave number range of 0.03–0.08 km^{-1}. Larger wave numbers (smaller wavelengths) are not considered because they are likely from noises and they are not needed according to our numerical and theoretical tests (Figures 1–4).

[30] First, we calculate Z_b from both EMAG2 and EMAG3 using a moving window of 208.8 × 208.8 km^2 in size and a moving step of 69.6 km (Figure 7). For each data set, a total of 10,425 Z_b are estimated with reference to the sea level. The general Z_b patterns from these two models are quite similar, with the majority of Z_b being located between 5 and 40 km beneath the sea level, and the mid-Atlantic ridge (MAR) showing mostly the shallowest Curie isotherm approaching the seafloor. Major intraplate hotspot such as BR, CI, and CVI all show well-defined small Z_b estimated from both EMAG2 and EMAG3. On average, Z_b values estimated from EMAG2 appear to be more uniform in the ridge-parallel directions, but they are even slightly smaller than those from EMAG3, despite the direction smoothing along the isochrons in EMAG2. These observations confirm that the directional gridding applied in EMAG2 does not cause significant biases in detected Z_b but does increase ridge-parallel uniformity.

[31] Local Z_b differences do occur from these two magnetic models. Most noticeable are some localized areas in the southwest with very small Z_b estimated from EMAG3 (Figure 7b), but these localized features do not exist in the Z_b map from EMAG2 (Figure 7a). From studying EMAG3, we notice that these Z_b anomalies accompany high-amplitude variations in magnetic anomalies. However, whether these magnetic and Z_b anomalies from EMAG3 are caused by true geological structures are uncertain, and these anomalies do not correspond directly with noticeable bathymetric features. In the gridding of EMAG2, each pair of magnetic values with gradient exceeding 3% between the two points on a track is discarded to avoid contamination by magnetic anomalies due to sea mounts [*Maus et al.*, 2009]. This procedure has removed from EMAG2 local magnetic and Z_b anomalies that are seen in EMAG3.

[32] We then estimate Z_b based on EMAG2 only, using two other different sizes of moving windows, in 104.4 × 104.4 and 156.6 × 156.6 km^2, respectively, and the moving step is kept at 52.2 km. The number of windows in which radial spectra and Z_b are estimated exceeds 18,000 for each run (Figure 8). A smaller moving window will give a higher Z_b resolution but may underestimate larger Z_b [*Chiozzi et al.*, 2005; *Ravat et al.*, 2007] and disguises regional features. A larger moving window leads to a lower resolution but gives more emphases on regional trends. Therefore, the use of three different moving windows put better constraints on Z_b, and the four Curie-depth maps (Figures 7 and 8) are complementary to one another. We observe again that the majority of Curie points are located between 5 and 40 km beneath the geoid, and the MAR corresponds exactly with a belt of smallest Z_b, approaching the seafloor depths. This verifies the accuracy of our methodology of estimating Z_b.

[33] Roughly along the two 45 Ma isochrons, there are two noticeable belts of shallow Z_b, which are subparallel to the MAR and span throughout North Atlantic, though less noticeable southward. To the north of the Charlie Gibbs Fracture Zone, high thermal anomalies do appear around Iceland, but neither Iceland itself nor the proximal Jan Mayen microcontinent and the Iceland transverse ridge (including the Greenland-Iceland and Iceland-Faeroe ridges, abbreviated as GIR and IFR, respectively) are anomalously hot, especially on the Z_b map estimated from EMAG2. This may explain why Iceland shows no evidence for significantly higher temperatures associated with a
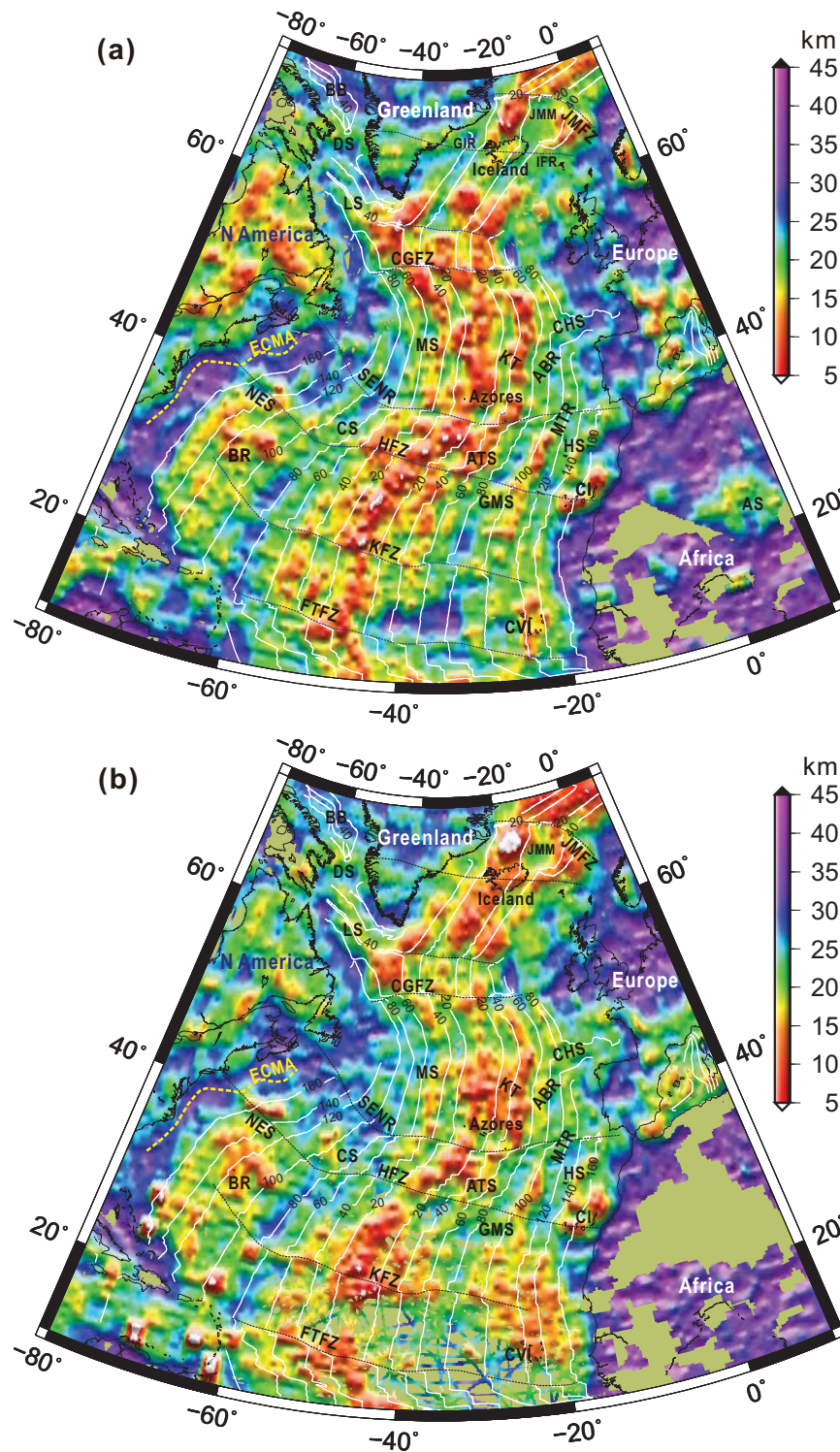
Figure 7. (a) Z_b map based on magnetic anomalies from EMAG2. (b) Z_b map based on magnetic anomalies from EMAG3. Both maps are in Albers equal-area conic projection and calculated with a window size of 208.8×208.8 km^2 and $\beta^p_{3D} = 3.0$. This odd fractional number of window size is selected with no special purpose but just for computing efficiency. Our original gridding interval is 2.9 km. To form a computing window of about 200 km wide, we choose 72×72 grids, leading to a window size of 208.8×208.8 km^2. The number 72 is a good choice because it can be accurately divided by 2 or 3, forming exact moving steps of a half or one third of the window width. For the same reason we have also selected windows of 104.4×104.4 and 156.6×156.6 km^2 in sizes in Figure 8. See Figure 1 for more annotations.
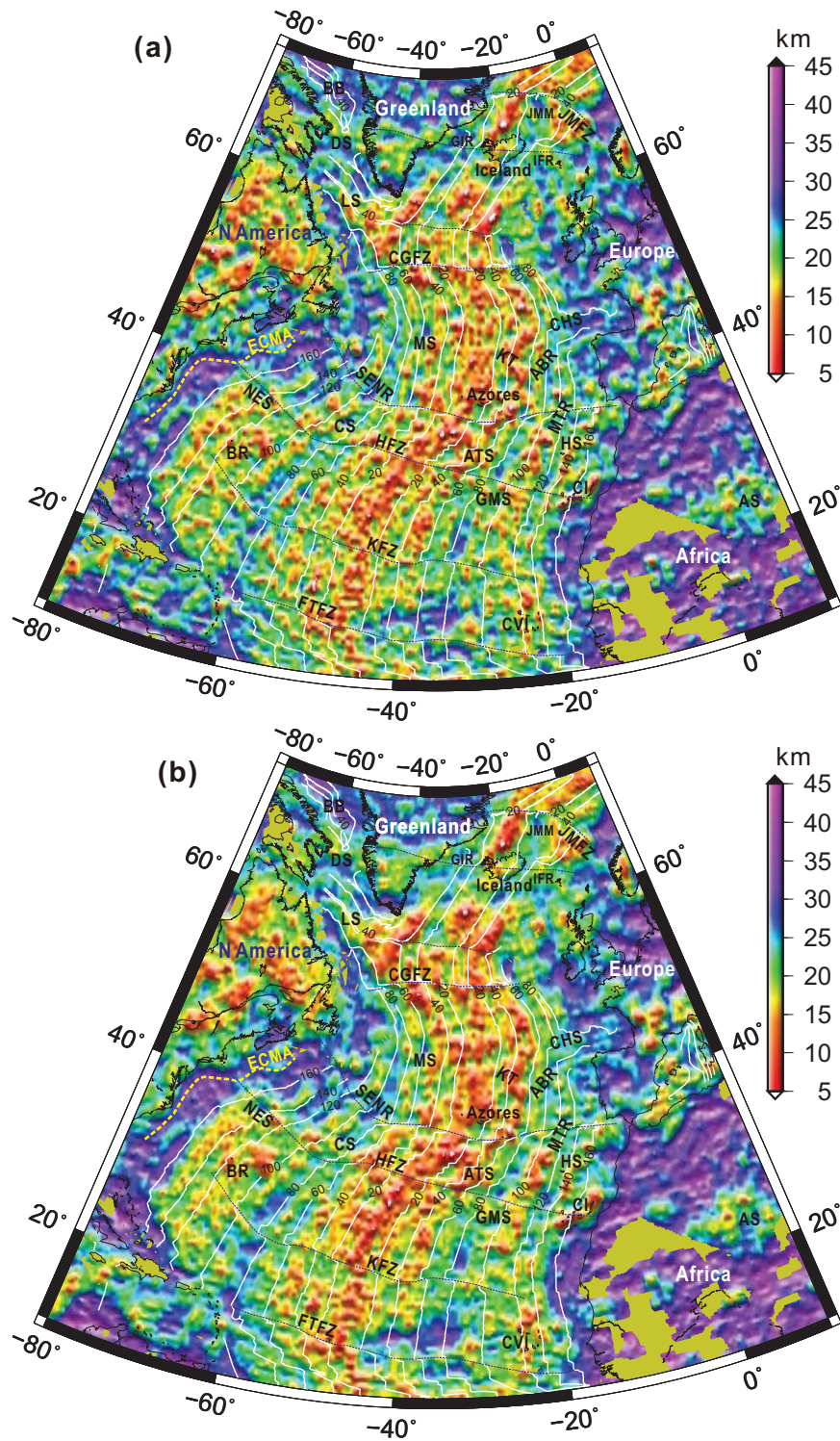
Figure 8. Maps of estimated Z_b in Albers equal-area conic projection. (a) Z_b calculated with a window size = 104.4 × 104.4 km^2. (b) Z_b calculated with a window size = 156.6 × 156.6 km^2. β_{3D}^p =3.0. Crustal isochrons are based on *Müller et al.* [2008]. Blue dashed lines are fracture zones. Yellow dashed line marks the ECMA, and its position is interpreted from Figure 1b. Fracture zones are interpreted from Figure 1. See Figure 1 for more annotations.

mantle plume [*Stein and Stein*, 2003] and leaves further speculations on whether the Icelandic lithosphere is rather colder than hotter [*Menke and Levin*, 1994; *Menke et al.*, 1995; *Foulger et al.*, 2003], and whether Iceland is associated with a geochemical or a thermal anomaly [*Anderson*, 2005; *Foulger*, 2012]. There are also other uncertainties and difficulties in interpreting estimated bottom of magnetic sources beneath Iceland, arising from a deep Moho serving likely as a local magnetic boundary, and from possible changes in the fractal parameter, in the Curie temperature due to a geochemical anomaly, and/or in the magnetic data specifications.

[34] Another near-ridge hotspot Azores shows neither anomalously shallow nor deep Z_b than most other near-ridge areas. Neither Iceland nor Azores demonstrates visible tracks of presumed plume trails on the Z_b map. In contrast, some of the major intraplate hotspots, such as the BR, the CVI, the CI, and the Ahaggar Swell in North Africa, show elevated Curie points in well-defined areas corresponding to their geographical extents (Figures 1, 7, and 8), confirming high thermal anomalies associated with these volcanic features. Although it remains unclear simply from our estimated Z_b, whether or not these hotspots are caused by deep mantle plumes, our new results do show a wide spectrum of different temperature anomalies, suggesting quite different mechanisms of origin. Comparatively, many of the small and submerged seamounts (e.g., Atlantis, Charcot, Corner, Great Meteor, Milne, and New England seamounts) do not show well-defined Z_b anomalies (Figures 1, 7, and 8).

6. Geothermal Evolution

6.1. Heat Flow Versus Crustal Ages

[35] The intriguing patterns of North Atlantic Z_b raise questions on the thermal evolution of the region. Z_b is a good proxy of subsurface temperature of about 550°C [e.g., *Mayhew*, 1982; *Tselentis*, 1991], if lateral compositional variations exert neglectable influence on the Curie temperature. One of the advantages of incorporating Z_b is that it provides a direct assessment of the current geothermal state of a lithosphere with a long period of evolution. This additional geothermal constraint translates virtually a 2-D time-dependent heat conduction problem to a 1-D steady heat conduction problem because Z_b records the lithospheric cooling effect. Therefore, the complexities in computing geotherms are very much reduced.

[36] A total number of 7087 heat-flow measurements are available in the study area from the Global Heat Flow Database of the International Heat Flow Commission (http://www.heatflow.und.edu/) last updated in January 2011. These new data are gridded in a constant 1° interval using the algorithm of minimum curvature with a tension factor of 0.5 (Figure 9). Heat-flow maps should be interpreted with caution because of the sparseness of the data, but Figure 9 resolves portions of the MAR very well with high heat flow. Even in areas with only sparse heat-flow measurements such as the northwestern Africa (lower right corner of Figure 9) and Greenland and northeastern North America (upper left corner of Figure 9), our gridded result is very similar in large-scale features to the surface-heat-flow model of *Shapiro and Ritzwoller* [2004], which uses the global 3-D shear velocity model of the crust and upper mantle of *Shapiro and Ritzwoller* [2002] to extrapolate existing heat-flow measurements of *Pollack et al.* [1993] to regions where such measurements are rare or absent. Elsewhere, the distribution of heat-flow points is very reasonable, and our results show a higher resolution than previous models in North Atlantic. For example, unlike the model of *Shapiro and Ritzwoller* [2004], we demonstrate high heat flow in the large area around the Bermuda Rise, and the dense heat-flow measurements there cannot make interpolation aliases.

[37] Figure 9 shows that neither the Iceland nor the Azores hotspot shows anomalously higher heat flow than other ridge segments, similar to that revealed by the Z_b maps. There is an overall decrease in heat flow from the ridge axis to the isochron 80 Ma; however, heat-flow variations are much more heterogeneous than any simple theoretical models can predict (Figure 9). There, in general, appears to have high heat flow between isochrons 0 and 60 Ma, a pattern similar to anomalously shallow Curie points in the same zone identified on the Z_b maps.

[38] For crust older than 80 Ma, more complexities in heat-flow variations occur. The three major intraplate hotspots (i.e., Bermuda Rise, Canary Islands, and Cape Verde Islands) and their proximities are accompanied with higher than normal heat flow. Removal of these anomaly spots does not produce a heat-flow versus age variation conformable to theoretical models, and strong heterogeneities persist. To the west of the MAR, between the Hayes Fracture Zone and the Southeast Newfoundland Ridge, a low heat-flow patch contrasts largely to an area of high heat flow
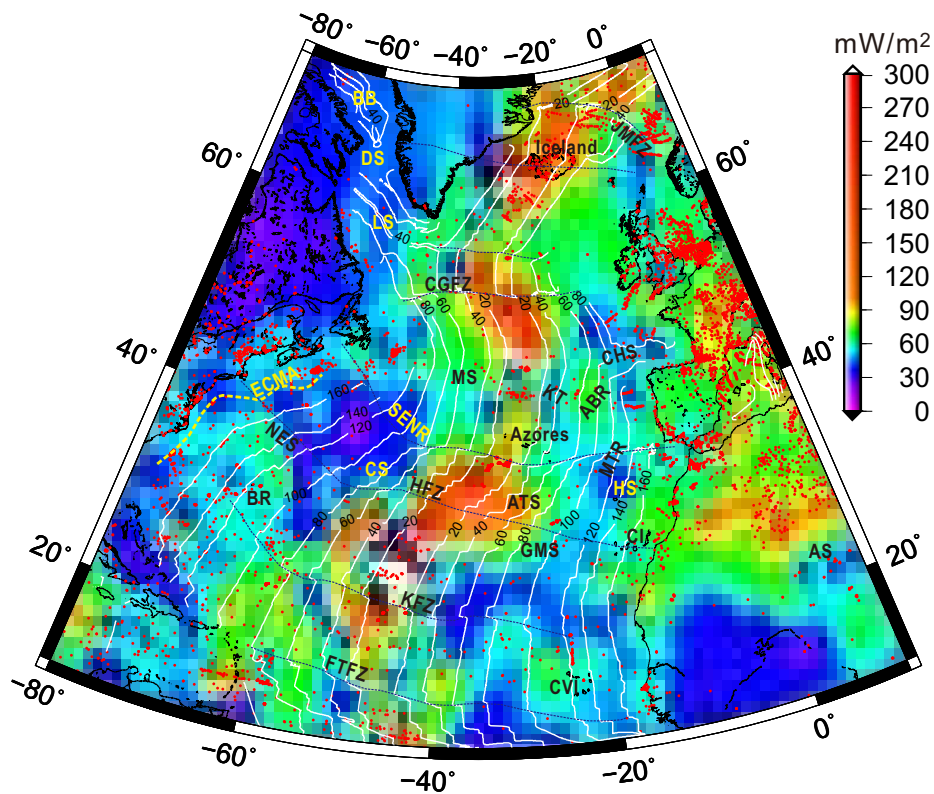
Figure 9. Heat-flow map of North Atlantic. Data points are gridded with a 1° interval. Red dots show the positions of heat-flow measurements. See Figure 1 for more annotations.

associated with the Bermuda Rise to the south, despite the similar ages of these two areas.

[39] The traditional way of studying the cooling of oceanic lithosphere is to plot all heat-flow measurements versus ages together in a single 2-D diagram. Figure 10 shows two versions of this diagram. The first is a raw plot showing all heat-flow measurements versus ages (Figure 10a), without any heat-flow interpolations. Because of the sparseness and irregularity in heat-flow measurement, this plot shows clustering of data points. In addition, we see a large number of very low heat-flow points located within very young oceanic crust (<20 Ma), caused primarily by hydrothermal circulation. In the second plot (Figure 10b), we use heat flow gridded in a constant 1° interval as shown in Figure 9. In this gridding process, all heat-flow data are considered, i.e., without excluding locally extremely high heat flow caused by focused flow of hot seawater from hydrothermal circulation and locally extremely low heat flow cooled by infiltration of cold dense seawater. We can see now that very low heat-flow points from very young oceanic crust are effectively eliminated and the data points become much more

coherent. *Hasterok et al.* [2011] recently corrected heat-flow data for sediments and seamounts in order to achieve a much higher correlation coefficient with seafloor age. Here we do not correct heat-flow data for sediments and seamounts by applying filtering, but the fit with seafloor age is still improved simply by large-grid interpolation. This is understandable, because large-grid interpolation of almost random heat-flow measurements captures the gross average heat fluxes of shallow oceanic crust, which are at the end mostly due to thermal conduction, no matter how and whether the measurements are affected locally by hydrothermal cooling or heating.

[40] Because almost all heat-flow measurements within crust older than 100 Ma are above the half-space cooling curve (Figure 10), even elimination of high heat flow associated with isolated intraplate hotspots (Bermuda Rise, Canary Islands, and Cape Verde Islands), as identified earlier, cannot allow the half-space cooling curve to fit the observations. In other words, mechanisms other than hotspot/plume heating have caused the deviation of heat-flow measurements from the half-space cooling model for old crust. The 2-D heat-flow
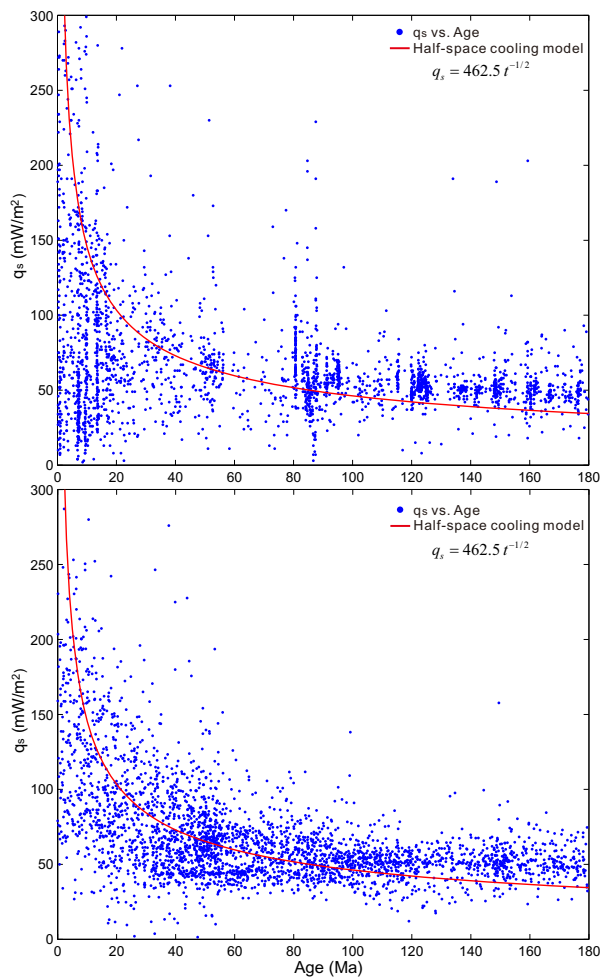
Figure 10. (a) Plot of original heat flow (q_s) versus crustal ages. (b) Plot of gridded heat flow (q_s) versus crustal ages. Red curves show predicted heat flow from the half-space cooling model.

versus age plot offers easy comparison between theoretical models and observations, but it virtually smears out the large lateral heterogeneities identified from the regional heat-flow map (Figure 9). In this regard, even though the plate model seems to be able to explain the apparent flattening in heat-flow observations in the 2-D plot, it cannot explain all heat-flow variations such as high and low heat-flow patches within old crust (>100 Ma).

6.2. Curie Depths Versus Crustal Ages

[41] The plot of Curie depths (Z_b) versus crustal ages (t) shows that Z_b increases in general with crustal ages (t) but has marked oscillations after ~40 Ma (Figure 11). This oscillatory pattern persists in profiles of Z_b extracted between major transform faults (Figures 11a–11d). If all data are

fitted in the least squares sense with the half-space cooling model, we have

$$Z_b = 1.677\sqrt{t} + 5.0. \qquad (7)$$

[42] Using the half-space sudden cooling solution [*Turcotte and Schubert*, 2002], and assuming temperatures of the lithospheric top and bottom to be 5°C and 1300°C, respectively, equation (7) yields a thermal diffusivity κ of 0.145 mm^2/s or 4.57 km^2/Ma, which appears to be too small comparing to known values. Although this fit seems to capture the overall data trend, noticeably there is a poor fit for ages less than 40 Ma where most observed Z_b deepens faster than the fitting curve.

[43] Alternatively, we optimally fit only data between 0 and 40 Ma and get

$$Z_b = 2.488\sqrt{t} + 5.0, \qquad (8)$$

which gives an average thermal diffusivity κ of the North Atlantic lithosphere of 0.319 mm^2/s or 10.06 km^2/Ma, a more reasonable estimate. As will be demonstrated in the next subsection, the effective thermal conductivity K is estimated at around 2.0 W/(m °C) from the Z_b versus heat-flow plots (Figure 12). Plugging these values of K and κ into the heat-flow equation of the half-space cooling model [*Parsons and Sclater*, 1977], and assuming the surface temperature is 0°C and the asthenospheric temperature is 1300°C, we have

$$q_s = 462.5t^{-1/2}, \qquad (9)$$

in which q_s is the heat flow in mW/m^2 and t is in Ma. It is seen that for crust younger than 100 Ma, this model (equation (9)) can fit well the interpolated heat flow despite larger scattering (Figure 10b), but most of the originally observed heat-flow points fall below this curve (Figure 10a). This difference indicates again that regional interpolation of heat-flow measurements (Figure 9) provides a much more meaningful constraint on deep geothermal field than the originally measured heat flow that bears more local disturbances.

[44] It has been long recognized that the half-space cooling model [*Parker and Oldenburg*, 1973] is not valid for ages beyond 80 Ma, and in general for old crust [e.g., *Crosby et al.*, 2006]. With this new fit, essentially almost all our Curie points within crust older than 40 Ma are shallower than the half-space cooling curve and with large noticeable undulations. The older is the oceanic
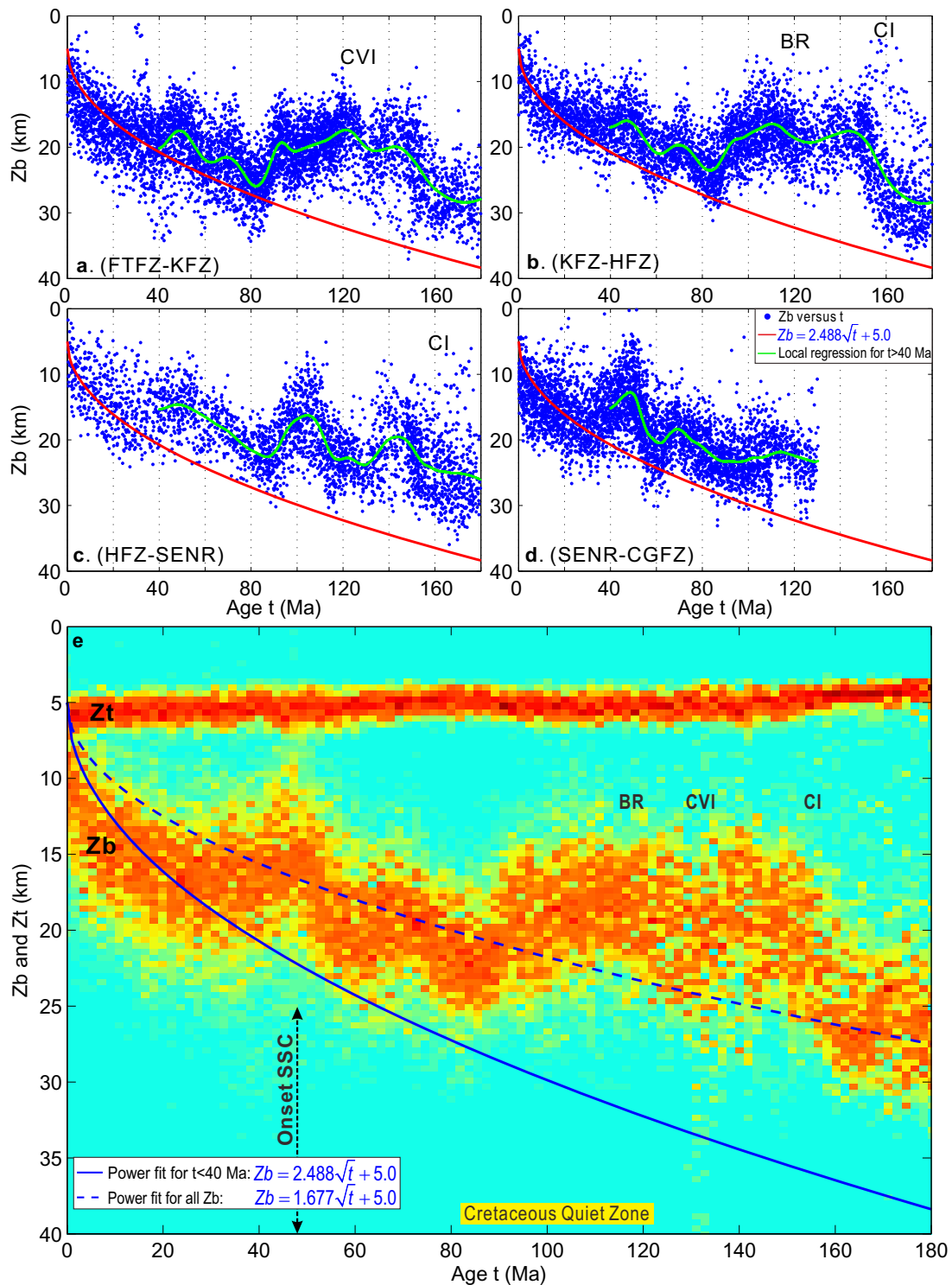
Figure 11. Z_b versus crustal ages (t) for different zones. (a) Data between FTFZ and KFZ, (b) data between KFZ and HFZ, (c) data between KFZ and SENR, (d) data between SENR and CGFZ, and (e) density plot of all data. Green trends in Figures 11a–11d are from locally weighted scatterplot smooth using linear least squares fitting and a second-degree polynomial. Z_b is estimated using three different moving window sizes (104.4×104.4, 156.6×156.6, and 208.8×208.8 km^2).
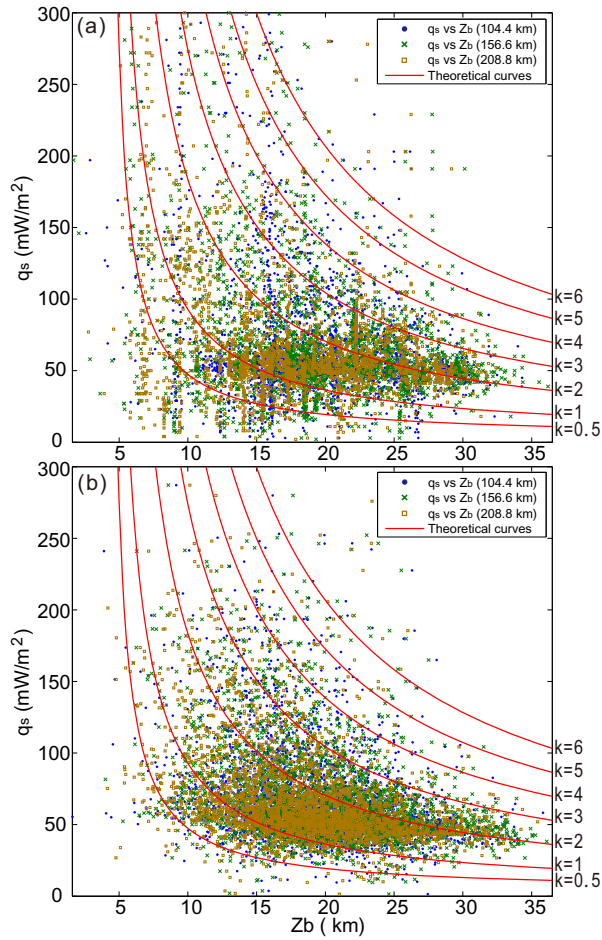
Figure 12. Plots of Z_b estimated with three different moving windows (104.4×104.4, 156.6×156.6, and 208.8×208.8 km^2) versus (a) original heat flow and (b) gridded heat flow. Numerical numbers in the legend are widths of squared moving windows. Red curves show the theoretical model of equation (10) with different thermal conductivities.

crust, the larger the deviations between Z_b and the model (Figure 11). In particular, there is no appreciable deepening in Curie points from the isochrons 80 to 160 Ma. Instead, between these two isochrons, the estimated Curie points are slightly elevated. More interestingly, the major active hotspots (BR, CI, and CVI) are all located within this zone of elevated Curie points. The elevated Curie depths around the BR aligned very well with the shallow bathymetry there (Figures 1 and 6). However, we did not observe noticeable flattening in Z_b at older ages that would be suggested by the plate model [*Parsons and Sclater*, 1977]. Thus, from both heat flow and Curie depths, we conclude that neither the half-space cooling model nor the plate model can fit our observations.

6.3. Curie Depths Versus Heat Flow

[45] Comparison between the q_s (Figure 9) and Z_b (Figures 7 and 8) shows similarities but also differences. We now study how heat flow is correlated globally with estimated North Atlantic Z_b. Similar to our studies of heat flow versus ages, we plot both raw and gridded heat-flow data versus Z_b (Figure 12). First, we interpolate and sample Z_b at the irregular positions of all heat-flow measurements and plot them in Figure 12a. Second, we interpolate heat flow and extract them at the all positions where we estimated Z_b and plot them in Figure 12b. As expected, raw heat-flow points are more scattered, mostly caused by very low heat-flow values. With heat-flow interpolation, the data points are much more coherent and show better trend conformable to theoretical curves.

[46] To plot the theoretical curves overlapped on the data points, we assume that heat production in the lithosphere is continuous and decreases exponentially with depth, and that at the Curie-point depth the temperature is fixed at the Curie temperature T_c, while the temperature is T_0 at the surface elevation Z_s. With these assumptions, surface heat flow q_s is related to Z_b, via [*Li*, 2011]

$$q_s = K \frac{T_c - T_0}{Z_b - Z_s} + h_r^2 H_0 \frac{e^{-Z_b/h_r} - e^{-Z_s/h_r}}{Z_b - Z_s} + h_r H_0 e^{-Z_s/h_r}, \quad (10)$$

where K is the thermal conductivity of the magnetic layer, H_0 is the heat production rate at the surface, and h_r is the characteristic dropoff of heat production. Equation (10) shows a nonlinear inverse relationship between heat flow and Z_b. For oceanic lithosphere, radioactive heat production is very low, so we assume $H_0 = 1.37$ μW/m^3 and $h_r = 5.0$ km, which are relatively small values making radioactive contributions to surface heat flow almost neglectable [*Turcotte and Schubert*, 2002]. Theoretical curves (equation (10)) with different K ranging from 0.5 to 6.0 W/(m °C) are plotted on Figure 12 against observed data. Interpolated heat-flow points, showing a more coherent trend, are better fitted by equation (10), when compared to raw heat-flow points.

[47] From Figure 12, we assess that the best fitting K is around 2.0 W/(m °C) for $Z_b > 20$ km, but for smaller Z_b, this K can be as high as 3.0 W/(m °C). The slightly decrease in K with increasing Z_b can be explained by the temperature dependence of K [*Whittington et al.*, 2009]. When studying Figure 12, we should look at the point distribution in the Z_b–q_s space rather than at density of point

clustering only. The apparent clustering of points around 60 mW/m^2 is simply because that is the average of heat flow, and there are simply more heat-flow measurements around the average. K so estimated represents the effective average thermal conductivity for the magnetic layer of North Atlantic but is also conformable to known measurements of oceanic basalts, gabbros, and peridotites recovered from Ocean Drilling Program cores [*Fitton et al.*, 2004; *Shipboard Scientific Party*, 2004].

6.4. Curie Depths Versus the Moho

[48] The relationship between the Curie and Moho interfaces is an interesting geodynamic problem, because the depth of the Curie isotherm (or equivalently the bottom of the magnetic layer) may indicate whether and how the uppermost mantle can be magnetized. Previous studies in western Pacific marginal seas (the South China Sea and the Shikoku Basin) have shown that Curie points are mostly located beneath the Moho and suggested the uppermost mantle of these oceanic basins is also magnetized and contributes to surface magnetic anomalies [*Li et al.*, 2010, 2012; *Li*, 2011]. These marginal basins are young but their spreading activities no longer exist. It will be very important to further testify these findings in areas that have active spreading and cover a wide range of crustal ages, and North Atlantic suits this purpose very well.

[49] To locate the Moho, residual mantle Bouguer anomalies of North Atlantic are first derived from using combinations of seafloor bathymetry [*Smith and Sandwell*, 1997], crustal ages [*Müller et al.*, 2008], free-air gravity [*Sandwell and Smith*, 2009], and sediment thickness [*Divins*, 2009], and crustal thickness models are then obtained from residual mantle Bouguer anomalies [*Wang et al.*, 2011].

[50] Most of the estimated Moho depths in the study area are less than 15 km below the geoid but have large lateral variations (Figure 13a). Along the MAR, Moho depths can increase considerably at places where on-axis hotspots (Azores and Iceland) are developed. In particular, Iceland and the Iceland transverse ridge (GIR and IFR) show Moho depths as large as 25 km, which appear to correlate with the anomalously deep Curie points there (Figures 7 and 8). Almost all seamounts and hotspots in North Atlantic are accompanied with significantly deepened Moho.

[51] To study their relationships, we simply subtract Moho depths from Curie depths and plot the depth difference in Figure 13b. Therefore, negative values in Figure 13b indicate that the Curie isotherm is above the Moho, and vice versa. Alternatively, Figure 13 can be viewed approximately as the isopach map of the magnetized uppermost mantle, and as an indirect measure of the Moho temperature or how the Moho temperature deviates from the Curie temperature. Figure 13b shows that the Curie isotherm is located mostly beneath the Moho, suggesting that the Moho here cannot be a magnetic boundary, and the uppermost mantle should also be magnetized and contributes to surface magnetic anomalies, as found in other oceanic basins [*Li et al.*, 2010; *Li*, 2011]. However, around major intraplate hotspots (BR, CI, and CVI), the Curie isotherm is anomalously shallow and often above the Moho. For oceanic crust younger than 50 Ma, the two interfaces tend to approach to each other, but again, a large variability exists. The magnetized layer in uppermost mantle tends to grow in thicknesses with ages, with exceptions around seamounts and hotspots. The two anomalous belts of small Z_b also cause the Curie isotherm to approach the Moho around the 45 Ma isochrons.

[52] How could the uppermost mantle be magnetized? Of course, cooling below the Curie point is the prerequisite for magnetization of mantle minerals. However, fresh mantle minerals are known to be of little susceptibility [*Wasilewski et al.*, 1979; *Wasilewski and Mayhew*, 1992]. Therefore, the magnetite-bearing serpentinites from hydration of upper mantle minerals are good candidates for triggering uppermost mantle magnetization. Implications for in situ uppermost mantle serpentinization from infiltration of seawater through large transform faults have been documented from both geochemical and geophysical studies [e.g., *Dyment et al.*, 1997; *Li and Lee*, 2006; *Delescluse and Chamot-Rooke*, 2008]. *Dyment et al.* [1997] showed that serpentinization of the uppermost mantle significantly contributes to marine magnetic anomalies in slow spreading ocean based on analyses of skewness of marine magnetic anomalies.

[53] If the uppermost mantle magnetization could result entirely from serpentinization, the magnetized and serpentinized layer shown in Figure 13b should have had a significant effect on surface heat flow and seafloor topography. This is because that serpentinization reactions produce volatiles such as methane and hydrogen, generate heat [*Fyfe*, 1974; *Lowell and Rona*, 2002; *Fruh-Green et al.*, 2003; *Emmanuel and Berkowitz*, 2006],
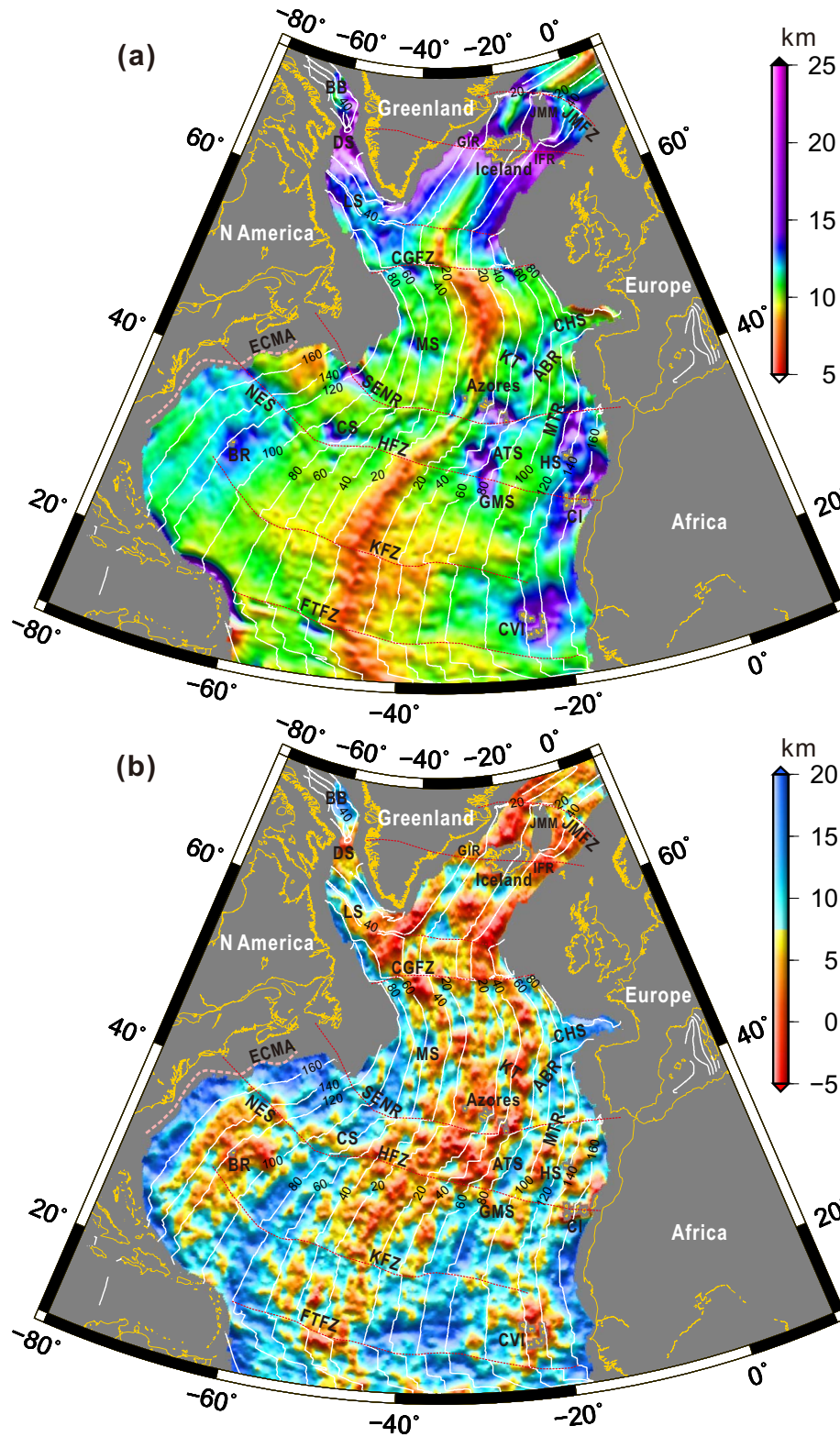
Figure 13. (a) Moho depths (with reference to the geoid) from the crustal thickness model of *Wang et al.* [2011] with a low-pass filtering. (b) The depth difference after subtracting Moho depths from Curie depths. See Figure 1 for more annotations.

increase volume [*MacDonald and Fyfe*, 1985; *O'Hanley*, 1992], and decrease density/velocity [*Christensen*, 1966; *Saad*, 1969], solidus temperatures, [*Asimow et al.*, 2004] and mantle viscosity [*Hirth and Kohlstedt*, 1996]. Heat production from serpentinization is dependent on a wide range of parameters including temperature, reaction kinetics, deformation, and water circulation rate but can contribute to heat-flow anomalies above theoretical cooling models [*Emmanuel and Berkowitz*, 2006; *Delescluse and Chamot-Rooke*, 2008].

[54] From Figure 13, it is seen that serpentinized mantle volume varies with Z_b but tends to increase with ages and progressive conductive cooling except for places with upwelling convective cells and hotspots and seamounts. Therefore, heat production from serpentinization above Z_b can compensate conductive cooling and produce heat flow higher than predicted from the half-space cooling model (Figure 10). Effects from small-scale upwelling convective cells and hotspots can also be compensated by heat production from serpentinization, because wherever these features exist, thicknesses of serpentinized layer drop significantly. Collectively, the compensation effects of serpentinization in heat production and volume expansion may be one important mechanism producing apparent departures in heat flow and bathymetry from theoretical models in old oceanic crust.

7. Implications for Possible Small-Scale Sublithosperic Convection

[55] *Parsons and McKenzie* [1978] invoked small-scale sublithospheric convection (SSC) to explain the apparent flattening in both heat-flow versus age and bathymetry versus age curves of old oceanic lithosphere. Although theoretical, numerical, and laboratory studies have hinted at the ubiquitous existence of SSC in the upper mantle under various tectonic settings [*Petersen et al.*, 2010], the direct geophysical evidence for SSC has yet to be found [*Landuyt and Ierley*, 2012]. Surface heat flow, bathymetry, gravity, and geoid do not show so clear signatures of SSC as in numerical studies [*Buck*, 1985; *Davies*, 1988; *Korenaga and Korenaga*, 2008; *Korenaga*, 2009]. Consequently, their exact forms, onset time, and triggering conditions are still under debate. Other mechanisms, such as radioactive heating [*Forsyth*, 1977], shear stress heating [*Schubert et al.*, 1976], asthenospheric flow [*Phipps Morgan and Smith*, 1992], plumes

[*Davies*, 1988], and trapped heat [*Huang and Zhong*, 2005], have also been introduced to account for bathymetric and heat-flow flattening in old seafloors. There are also conflicting arguments on whether seafloor flattening persists, if hotspots and oceanic plateaus are removed [*Schroeder*, 1984; *Hillier and Watts*, 2005; *Korenaga and Korenaga*, 2008], or if the bathymetry is observed along mantle flow lines rather than along trajectories normal to isochrons [*Adam and Vidal*, 2010].

[56] The most interesting features we find are two belts of shallow Z_b that are roughly the 40 Ma isochrons and subparallel to MAR, mostly noticeable between 20°N and 60°N (Figures 7 and 8). Then, roughly along the 85 Ma isochrons, there are two belts of deep Z_b on both sides of MAR. Between the 90 and 160 Ma isochrons, Z_b is relatively shallow and does not show appreciable deepening with increasing ages.

[57] The overall Z_b variations seem to indicate a sublithospheric convective pattern with preferred transverse rolls subparallel to MAR. One may wonder whether magnetic anomaly lineups have contributed to these transverse patterns, but our well-resolved thermal anomalies of MAR and of known intraplate hotspots prove that our technique and result are independent of magnetic reversal frequencies. The wavelengths of detected thermal anomalies certainly differ greatly from wavelengths of magnetic anomalies. The introduction of fractal exponent in the inversion also effectively suppresses lateral correlations of magnetic sources [*Pilkington and Todoeschuck*, 1993, 1995; *Maus et al.*, 1997; *Ravat et al.*, 2007; *Bouligand et al.*, 2009] and leads to Z_b conformable to known geological constraints.

[58] Figure 11 further reveals that these noticeable oscillations in Z_b have an average period of ~30 Ma. Taking the average half-spreading rate of North Atlantic to be 16.4 mm/yr [*Müller et al.*, 2008], this translates to an average wavelength of ~492 km, which is close to scales of other suggested SSC [*Richter and McKenzie*, 1978; *Yuen and Fleitout*, 1985; *Anderson*, 1998; *van Hunen et al.*, 2005; *Ramsay and Pysklywec*, 2011]. This wavelength scale and the overall Z_b pattern are independent of window sizes applied. These oscillations in Z_b and therefore geotherms in the North Atlantic lithosphere are probably caused by upper mantle SSC.

[59] From Figure 11, we interpret that the onset time of North Atlantic SSC is ~40 Ma, when the first dripping instability starts to occur due to

cooling and gravity [*Dumoulin et al.*, 2005]. Numerical investigations suggest that the onset time is related physically to reactivation energy and Rayleigh number [*Huang and Zhong*, 2005], and geologically to inherited lithospheric base topography and partial melting [*Dumoulin et al.*, 2005]. The prominent thermal anomalies around 40 Ma may indicate a large amplitude of thermal perturbation from the onset of convection. Nevertheless, SSC alone appears not sufficient enough to cause the progressively larger departure in observed Z_b from the model. Other processes responsible for topographic flattening, such as mantle serpentinization discussed earlier, may also act in modifying Z_b.

[60] Considerable increases in Curie depths are observed near the continent-ocean boundary (COB), particularly in the oceanic lithosphere west of the BR, between the 160 Ma isochron and the East Coast Magnetic Anomaly (Figures 7 and 8). This indicates an intriguing scenario of the cooling and deep mantle processes of the North Atlantic COB. One possible explanation is that near the COB the old Atlantic oceanic lithosphere cools much faster since it is immediately adjacent to a relatively cold continent. Conversely, this can be interpreted as an oceanic crust of normal cooling but interacted with anomalous heating from mantle plumes or small-scale mantle convection between isochrons 160 and 80 Ma. The development of a downwelling cell of a small-scale edge-driven convection [*King and Anderson*, 1998; *King and Ritsema*, 2000; *King*, 2007; *Ramsay and Pysklywec*, 2011] can explain the accelerated cooling near the COB, the upwelling of the Bermuda Rise, and also possibly the volcanisms of Canary Islands and Cape Verde Islands (e.g., *Vogt*, 1991; *Ballmer et al.*, 2010). Though not completely in symmetry, similar Curie-depth patterns exists on conjugate COB of North Africa.

[61] The three major intraplate hotspots (BR, CVI, and CI) are located primarily in a zone of significantly elevated Curie points, corresponding roughly to the age period from ~90 to ~160 Ma (Figures 7, 8, and 11). The BR seems to correspond with a large upwelling convective cell. The CVI and CI may not be exactly on upwelling peaks but are almost certainly related to high thermal anomalies of adjacent upwelling cells. All these active intraplate hotspots show bathymetric highs that can be caused dynamically by convective upwelling and anomalously high temperatures, and localized volcanic conduits might be related to lithospheric fracturing.

[62] Convective patterns similar to that shown in Figure 11 have been demonstrated by numerical modeling [*Davies*, 1988; *Huang and Zhong*, 2005; *Dumoulin et al.*, 2005; *Landuyt and Ierley*, 2012] but have not yet been so evident from direct geophysical observations. One possible reason is that changes in asthenosphere temperature are not synchronized with their surface manifestations, especially for thick lithosphere [*Korenaga*, 2009; *Foulger*, 2012]. Another is that the flexural rigidity may diminish the magnitude of dynamic topography [*Buck*, 1985]. Subaerial erosion, deposition, and hydrothermal circulations will also bias our observations. In this sense, deep lithospheric thermal inversions, based on either seismic tomography [*Ritzwoller et al.*, 2004] or isothermal depth estimation in this paper, have definitive advantages.

[63] The development of basinwide transverse rolls (Figure 11) implies that the lithospheric age is a primary factor in controlling North Atlantic SSC. Unlike previous studies in the Pacific and in numerical modeling that have suggested preferred longitudinal rolls [*Richter and Parsons*, 1975; *Haxby and Weissel*, 1986; *Harmon et al.*, 2011], our results demonstrate instead dominance of transverse rolls in North Atlantic. This contrast might be related to differences in spreading rates of the two oceans since the plate velocity can have a strong influence on the development of sublithospheric convection [*Landuyt and Ierley*, 2012]. The slow spreading rate of North Atlantic may not favor developing longitudinal rolls. Our next initiative is to study the Pacific Z_b and see whether and how spreading rate variations and hotspots affect Z_b there.

[64] It should be noted that there are some caveats and uncertainties of the methodology, which can complicate our interpretations of estimated Z_b. The bottom of magnetic sources detected by this methodology may not always correspond to the Curie temperature isotherm but may instead correspond to a lithologic contact, e.g., between crust and nonmagnetic mantle or between serpentinized and not serpentinized mantle. Curie temperature may vary from one area to another due to changes in mineralogy or titanium content. Results may be biased when the data include various surveys with different specifications. Although the fractal parameter can be constrained near the mid-ocean ridge, it is generally not known beforehand and may vary in space.

8. Conclusion

[65] Detecting lithospheric geotherms in ocean basins currently proves very difficult with only low-resolution shear wave velocities from seismic tomography and sparsely and irregularly spaced heat-flow measurements. Forward numerical modeling of oceanic lithospheric cooling cannot incorporate complex local variations. Curie-depth inversions from recently published global magnetic anomaly models open a new venue for detecting North Atlantic lithospheric thermal state. To calibrate the algorithms, we examine first two theoretical models (the Maus model and the Blakely model) of radial amplitude spectrum of magnetic anomalies. These two fractal magnetization models are derived with different assumptions of model parameters, but by a proper reformulation, they are nearly identical and can be used interchangeably. Both theoretical and numerical synthetic studies reveal that linearization of both models at proper wave number bands can give accurate estimates of depths to the top and bottom of the magnetic layer. Selection of small wave numbers for estimating centroid depths is particular critical because the required bandwidths are normally narrow and turn to be slightly narrower with increasing Curie depths. However, our synthetic modeling suggests that the largest error in estimated Curie depths using the linearized centroid method employed in this paper will not reach 35%, given that selected fractal exponent and wave number bands for linear regressions are reasonable.

[66] Our theoretical and synthetic studies demonstrate the importance of corrections for fractal exponents. Without this correction, the inversion scheme is not sensitive to Curie-depth variations and will give overestimations. Corrections will lead to accurate and well-resolved Curie depths. To suppress correlations and long wavelengths of shallow magnetizations, a constant fractal exponent $\beta_{3D}^p = 3$ is taken in the inversion. With this fractal exponent, estimated depths to the top and bottom of the magnetic layer near the mid-Atlantic ridge tend to converge and are nearly equal to basement depths of the oceanic basin, as expected. Therefore, our well-imaged thermal anomalies at the active North Atlantic spreading ridge provide an important benchmark for selecting fractal exponent and testing the robustness of this technique. Furthermore, we obtain well-resolved thermal anomalies associated with major intraplate hotpots. Both our theoretical and computational analyses confirm that the inversion scheme needs not to discriminate between induced or remanent magnetization and does not require reduction to the pole.

[67] North Atlantic Curie depths, estimated using three different window sizes, follow a general trend of increase with crustal ages, but large lateral heterogeneities exist, related possibly to small-scale convection and hotspots. Interpreted from Curie isotherm oscillations, transverse small-scale convective rolls may start to develop beneath the North Atlantic lithosphere older than 40 Ma and are thought to have disturbed lithospheric geotherms. Unlike dominant longitudinal rolls previously suggested in the Pacific, the slow spreading rates of North Atlantic may favor transverse convective patterns, which are so far largely ignored. The scales of identified convective rolls are averaged at about 500 km, suggesting that their developments are mainly in the upper mantle above the 670 km discontinuity.

[68] Hotspots show a wide spectrum of heat-flow and Curie-depth anomalies. Although with much deepened Moho, the two major on-axis hotspots, Iceland and Azores, show little Curie-depth and thermal anomalies compared to other parts of the mid-Atlantic ridge. Other intraplate hotspots, mainly BR, CI, and CVI, develop within regions with much elevated Curie points and show well-defined local high thermal anomalies corresponding exactly to their geographical extents. These hotspots correspond more likely to upwelling small-scale convective cells rather than to plumes.

[69] Despite their sparse and irregular distributions and large local variations, North Atlantic heat-flow measurements, after a 1° interval gridding, correlate well with Curie depths in large-scale features, with areas of elevated Curie points corresponding mostly to higher heat flow. The significance of interpolated heat flow can be better viewed from their correlations with crustal ages and Curie depths; interpolated heat-flow points have much better fit with ages according to the theoretical half-space cooling model (equation (9)), and with estimated Curie depths in light of the theoretical thermal conduction model (equation (10)). For the magnetic layer, these optimal fittings yield an average thermal diffusivity of 0.319 mm²/s or 10.06 km²/Ma and reveal that the effective thermal conductivity decreased roughly from around 3.0 W/(m °C) to around 2.0 W/(m °C) with increasing depths.

[70] The fact that most North Atlantic Curie points are located beneath the Moho suggests that the

uppermost mantle is also magnetized from serpentinization and contributes to surface magnetic anomalies, as also found in west Pacific marginal seas. Serpentinization reactions generate heat and volume expansion that are capable of compensating effects of conductive cooling, small-scale convection, and hotspot volcanisms and cause apparent heat-flow and bathymetric flattening and deviations from theoretical cooling models.

Acknowledgments

References

Adam, C., and V. Vidal (2010), Mantle flow drives the subsidence of oceanic plates, *Science*, *328*, 83–85.

Anderson, D. L. (1998), The scale of mantle convection, *Tectonophysics*, *284*, 1–17.

Anderson, D. L. (2005), Scoring hotspots: The plume and plate paradigms, in *Plates, Plumes, and Paradigms*, edited by G. R. Foulger et al., Geol. Soc. Am. Spec. Pap., *388*, 31–54.

Asimow, P. D., J. E. Dixon, and C. H. Langmuir (2004), A hydrous melting and fractionation model for mid-ocean ridge basalts: Application to the mid-Atlantic ridge near the Azores, *Geochem. Geophys. Geosyst.*, *5*, Q01E16, doi:10.1029/2003GC000568.

Ballmer, M. D., G. Ito, J. van Hunen, and P. J. Tackley (2010), Small-scale sublithospheric convection reconciles geochemistry and geochronology of 'superplume' volcanism in the western and south Pacific, *Earth Planet. Sci. Lett.*, *290*, 224–232.

Bansal, A. R., G. Gabriel, V. P. Dimri, and C. M. Krawczyk (2011), Estimation of depth to the bottom of magnetic sources by a modified centroid method for fractal distribution of sources: An application to aeromagnetic data in Germany. *Geophysics*, *76*, L11–L22.

Blakely, R. J. (1995), *Potential Theory in Gravity and Magnetic Applications*, pp. 1–464, Cambridge Univ. Press, Cambridge, UK.

Blakely, R. J., and S. Hassanzadeh (1981), Estimation of depth to magnetic source using maximum entropy power spectra with application to the Peru-Chile Trench, in *Nazca Plate: Crustal Formation and Andean Convergence*, Geol. Soc. Am. Mem., *154*, 667–682.

Bouligand, C., J. M. G. Glen, and R. J. Blakely (2009), Mapping Curie temperature depth in the western United States with a fractal model for crustal magnetization, *J. Geophys. Res.*, *114*, B11104, doi:10.1029/2009JB006494.

Buck, W. R. (1985), When does small scale convection begin beneath oceanic lithosphere?, *Nature*, *313*, 775–777.

Chiozzi, P., J. Matsushima, Y. Okubo, V. Pasquale, and M. Verdoya (2005), Curie-point depth from spectral analysis of magnetic data in central–southern Europe, *Phys. Earth Planet. Inter.*, *152*, 267–276.

Christensen, N. I. (1966), Elasticity of ultrabasic rocks, *J. Geophys. Res.*, *71*(24), 5921–5931, doi:10.1029/JZ071i024p05921.

Cordell, L., J. D. Phillips, and R. H. Godson (1993), USGS potential-field geophysical software for PC and compatible microcomputers, *Leading Edge*, *12*, 290.

Crosby, A. G., D. McKenzie, and J. G. Sclater (2006), The relationship between depth, age and gravity in the oceans, *Geophys. J. Int.*, *166*, 553–573.

Davies, G. F. (1988), Ocean bathymetry and mantle convection: 2. Small scale flow, *J. Geophys. Res.*, *93*(89), 10,481–10,488, doi:10.1029/JB093iB09p10481.

Delescluse, M., and N. Chamot-Rooke (2008), Serpentinization pulse in the actively deforming Central Indian Basin, *Earth Planet. Sci. Lett.*, *276*, 140–151.

Divins, D. L. (2009), *NGDC Total Sediment Thickness of the World's Oceans & Marginal Seas*, Mar. Geol. and Geophys., Boulder, Colo. [Available at http://www.ngdc.noaa.gov/mgg/sedthick/sedthick.html.].

Doin, M. P., and L. Fleitout (1996), Thermal evolution of the oceanic lithosphere: An alternate view, *Earth Planet. Sci. Lett.*, *142*, 121–136.

Dumoulin, C., M. P. Doin, L. Fleitout, and D. Arcay (2005), Onset of small scale instabilities at the base of the lithosphere: Scaling laws and role of pre-existing lithospheric structures, *Geophys. J. Int.*, *160*, 344–356.

Dyment, J., J. Arkani-Hamed, and A. Ghods (1997), Contribution of serpentinized ultramafics to marine magnetic anomalies at slow and intermediate spreading centres: Insights from the shape of the anomalies, *Geophys. J. Int.*, *129*, 691–701.

Emmanuel, S., and B. Berkowitz (2006), Suppression and stimulation of seafloor hydrothermal convection by exothermic mineral hydration, *Earth Planet. Sci. Lett.*, *243*, 657–668.

Fitton, J. G., J. J. Mahoney, P. J. Wallace, and A. D. Saunders (2004), Leg 192 synthesis: Origin and evolution of the Ontong Java Plateau, in *Proc. ODP, Sci. Results, 192*, edited by J. G. Fitton et al., pp. 1–18, Ocean Drill. Program, College Station, Tex.

Fleitout, L., and D. A. Yuen (1984), Steady-state, secondary convection beneath lithospheric plates with temperature-dependent and pressure-dependent viscosity, *J. Geophys. Res.*, *89*(B11), 9227–9244, doi:10.1029/JB089iB11p09227.

Forsyth, D. W. (1977), The evolution of the upper mantle beneath mid-ocean ridges, *Tectonophysics*, *38*, 89–118.

Foulger, G. R. (2012), Are 'hot spots' hot spots?, *J. Geodyn.*, *58*, 1–28.

Foulger, G. R., Z. Du, and B. R. Julian (2003), Icelandic-type crust, *Geophys. J. Int.*, *155*, 567–590.

Fruh-Green, G. L., D. S. Kelley, S. M. Bernasconi, J. A. Karson, K. A. Ludwig, D. A. Butterfield, C. Boschi, and G. Proskurowski (2003), 30,000 years of hydrothermal activity at the lost city vent field, *Science*, *301*, 495–498.

Fyfe, W. S. (1974), Heats of chemical reactions and submarine heat production, *Geophys. J. R. Astron. Soc.*, *37*, 213–215.

Hamoudi, M., E. Thébault, V. Lesur, and M. Mandea (2007), GeoForschungsZentrum Anomaly Magnetic Map (GAMMA): A candidate model for the World Digital Magnetic Anomaly Map, *Geochem. Geophys. Geosyst.*, *8*, Q06023, doi:10.1029/2007GC001638.

Harmon, N., D. W. Forsyth, D. S. Weeraratne, Y. Yang, and S. C. Webb (2011), Mantle heterogeneity and off axis volcanism on young Pacific lithosphere, *Earth Planet. Sci. Lett.*, *311*, 306–315.

Hassanzadeh, S. (1976), Determination of depth to the magnetic basement using maximum entropy with application to the Northern Chile Trench, MS thesis, pp. 1–64, Oregon State Univ., Corvallis, OR, USA.

Hasterok, D., D. S. Chapman, and E. E. Davis (2011), Oceanic heat flow: Implications for global heat loss, *Earth Planet. Sci. Lett.*, *311*, 386–395.

Haxby, W. F., and J. K. Weissel (1986), Evidence for small-scale convection from seasat altimeter data, *J. Geophys. Res.*, *91*(B3), 3507–3520, doi:10.1029/JB091iB03p03507.

Hemant, K., E. Thébault, M. Mandea, D. Ravat, and S. Maus (2007), Magnetic anomaly map of the world: Merging satellite, airborne, marine and ground-based magnetic data sets, *Earth Planet. Sci. Lett.*, *260*, 56–71.

Hillier, J. K., and A. B. Watts (2005), Relationship between depth and age in the North Pacific Ocean, *J. Geophys. Res.*, *110*, B02405, doi:10.1029/2004JB003406.

Hirth, G., and D. L. Kohlstedt (1996), Water in the oceanic upper mantle: Implications for rheology, melt extraction, and the evolution of the lithosphere, *Earth Planet. Sci. Lett.*, *144*, 93–108.

Huang, J., and S. Zhong (2005), Sublithospheric small-scale convection and its implications for the residual topography at old ocean basins and the plate model, *J. Geophys. Res.*, *110*, B05404, doi:10.1029/2004JB003153.

King, S. (2007), Hotspots and edge-driven convection, *Geology*, *35*, 223–226.

King, S., and D. Anderson (1998), Edge-driven convection, *Earth Planet. Sci. Lett.*, *160*, 298–296.

King, S., and J. Ritsema (2000), African hot spot volcanism: Small-scale convection in the upper mantle beneath cratons, *Science*, *290*, 1137–1140.

Korenaga, J. (2009), How does small-scale convection manifest in surface heat flux?, *Earth Planet. Sci. Lett.*, *287*, 329–332.

Korenaga, T., and J. Korenaga (2008), Subsidence of the oceanic lithosphere, apparent thermal expansivity, and seafloor flattening, *Earth Planet. Sci. Lett.*, *268*, 41–51.

Landuyt, W., and G. Ierley (2012), Linear stability analysis of the onset of sublithospheric convection, *Geophys. J. Int.*, *189*, 19–28.

Li, C.-F. (2011), An integrated geodynamic model of the Nankai subduction zone and neighboring regions from geophysical inversion and modeling, *J. Geodyn.*, *51*, 64–80.

Li, C.-F., B. Chen, and Z. Zhou (2009), Deep crustal structures of eastern China and adjacent seas revealed by magnetic data, *Sci. China (Ser. D)*, *52*, 984–993.

Li, C.-F., X. Shi, Z. Zhou, J. Li, J. Geng, and B. Chen (2010), Depths to the magnetic layer bottom in the South China Sea area and their tectonic implications, *Geophys. J. Int.*, *182*, 1229–1247.

Li, C.-F., J. Wang, Z. Zhou, J. Geng, B. Chen, F. Yang, J. Wu, P. Yu, X. Zhang, and S. Zhang (2012), 3D geophysical characterization of the Sulu-Dabie orogen and its environs, *Phys. Earth Planet. Inter.*, *192*, 35–53.

Li, Z.-X., and C.-T. A. Lee (2006), Geochemical investigation of serpentinized oceanic lithospheric mantle in the Feather River Ophiolite, California: Implications for the recycling rate of water by subduction, *Chem. Geol.*, *235*, 161–185.

Lowell, R. P., and P. A. Rona (2002), Seafloor hydrothermal systems driven by the serpentinization of peridotite, *Geophys. Res. Lett.*, *29*(11), 1531, doi:10.1029/2001GL014411.

MacDonald, A. H., and W. S. Fyfe (1985), Rate of serpentinization in seafloor environments, *Tectonophysics*, *116*, 123–135.

Maus, S., and V. Dimri (1995), Potential field power spectrum inversion for scaling geology, *J. Geophys. Res.*, *100*(B7), 12,605–12,616, doi:10.1029/95JB00758.

Maus, S., and V. P. Dimri (1994), Scaling properties of potential fields due to scaling sources, *Geophys. Res. Lett.*, *21*(10), 891–894, doi:10.1029/94GL00771.

Maus, S., D. Gordan, and D. Fairhead (1997), Curie-temperature depth estimation using a self-similar magnetization model, *Geophys. J. Int.*, *129*, 163–168.

Maus, S., T. Sazonova, K. Hemant, J. D. Fairhead, and D. Ravat (2007), National Geophysical Data Center candidate for the World Digital Magnetic Anomaly Map, *Geochem. Geophys. Geosyst.*, *8*, Q06017, doi:10.1029/2007GC001643.

Maus, S., et al. (2009), EMAG2: A 2-arc-minute resolution Earth Magnetic Anomaly Grid compiled from satellite, airborne and marine magnetic measurements, *Geochem. Geophys. Geosyst.*, *10*, Q08005, doi:10.1029/2009GC002471.

Mayhew, M. A. (1982), Application of satellite magnetic anomaly data to Curie isotherm mapping, *J. Geophys. Res.*, *87*(B6), 4846–4854, doi:10.1029/JB087iB06p04846.

Menke, W., and V. Levin (1994), Cold crust in a hot spot, *Geophys. Res. Lett.*, *21*(18), 1967–1970, doi:10.1029/94GL01896.

Menke, W., V. Levin, and R. Sethi (1995), Seismic attenuation in the crust at the mid-Atlantic plate boundary in south-west Iceland, *Geophys. J. Int.*, *122*, 175–182.

Müller, R. D., M. Sdrolias, C. Gaina, and W. R. Roest (2008), Age, spreading rates, and spreading asymmetry of the world's ocean crust, *Geochem. Geophys. Geosyst.*, *9*, Q04006, doi:10.1029/2007GC001743.

O'Hanley, D. S. (1992), Solution to the volume problem in serpentinization, *Geology*, *20*, 705–708.

Okubo, Y., R. J. Graf, R. O. Hansen, and M. Fytikas (1985), Curie point depths of the Island of Kyushu and surrounding areas, Japan, *Geophysics*, *53*, 481–494.

Parker, R. L., and D. W. Oldenburg (1973), Thermal model of ocean ridges, *Nature*, *242*, 137–139.

Parsons, B., and D. McKenzie (1978), Mantle convection and thermal structure of plates, *J. Geophys. Res.*, *83*(B9), 4485–4496, doi:10.1029/JB083iB09p04485.

Parsons, B., and J. G. Sclater (1977), An analysis of the variation of ocean floor bathymetry and heat flow with age, *J. Geophys. Res.*, *82*(5), 803–827, doi:10.1029/JB082i005p00803.

Petersen, K. D., S. B. Nielsen, O. R. Clausen, R. Stephenson, and T. Gerya (2010), Small-scale mantle convection produces stratigraphic sequences in sedimentary basins, *Science*, *329*, 827–830.

Phillips, J. D. (1997), Potential-Field Geophysical Software for the PC, version 2.2, Open-File Rep., 97–725, http://pubs.usgs.gov/of/1997/ofr-97-0725/.

Phipps Morgan, J., and W. H. F. Smith (1992), Flattening of the seafloor depth-age curve as a response to asthenospheric flow, *Nature*, *359*, 524–527.

Pilkington, M., and J. P. Todoeschuck (1993), Fractal magnetization of the continental crust, *Geophys. Res. Lett.*, *20*(7), 627–630, doi:10.1029/92GL03009.

Pilkington, M., and J. P. Todoeschuck (1995), Scaling nature of crustal susceptibilities, *Geophys. Res. Lett.*, *22*(7), 779–782, doi:10.1029/95GL00486.

Pollack, H. N., S. J. Hurter, and J. R. Johnson (1993), Heat flow from the Earth's interior: Analysis of the global data set, *Rev. Geophys.*, *31*(3), 267–280, doi:10.1029/93RG01249.

Purucker, M. E. (2007), Magnetic anomaly map of the world, *Eos Trans. AGU*, *88*(25), 263.

Purucker, M. E., and D. A. Clark (2011), Mapping and interpretation of the lithospheric magnetic field, in *Geomagnetic Observations and Models*, edited by M. Mandea and M. Korte, IAGA Spec. Sopron Book Ser. 5, pp. 311–338, Springer, Netherlands.

Purucker, M. E., and K. Whaler (2007), Crustal magnetism, in *Geomagnetism, vol. 5, Treatise on Geophysics*, edited by M. Kono, chap. 6, pp. 195–237, Elsevier.

Ramsay, T., and R. Pysklywec (2011), Anomalous bathymetry, 3D edge driven convection, and dynamic topography at the western Atlantic passive margin, *J. Geodyn.*, *52*, 45–56.

Ravat, D., A. Pignatelli, I. Nicolosi, and M. Chiappini (2007), A study of spectral methods of estimating the depth to the bottom of magnetic sources from near-surface magnetic anomaly data, *Geophys. J. Int.*, *169*, 421–434.

Richter, F. M., and D. McKenzie (1978), Simple plate models of mantle convection, *J. Geophys.*, *44*, 441–471.

Richter, F. M., and B. Parsons (1975), On the interaction of two scales of convection in the mantle, *J. Geophys. Res.*, *80*(17), 2529–2541, doi:10.1029/JB080i017p02529.

Ritzwoller, M. H., N. M. Shapiro, and S. Zhong (2004), Cooling history of the Pacific lithosphere, *Earth Planet. Sci. Lett.*, *226*, 69–84.

Saad, A. F. (1969), Magnetic properties of ultramafic rocks from Red Mountain, California, *Geophysics*, *34*, 974–987.

Sandwell, D. T., and W. H. F. Smith (2009), Global marine gravity from retracked Geosat and ERS-1 altimetry: Ridge segmentation versus spreading rate, *J. Geophys. Res.*, *114*, B01411, doi:10.1029/2008JB006008.

Schroeder, W. (1984), The empirical age-depth relation and depth anomalies in the Pacific Ocean basin, *J. Geophys. Res.*, *89*(B12), 9873–9883, doi:10.1029/JB089iB12p09873.

Schubert, G., C. Froidevaux, and D. A. Yuen (1976), Oceanic lithosphere and asthenosphere thermal and mechanical structure, *J. Geophys. Res.*, *81*(20), 3525–3540, doi:10.1029/JB081i020p03525.

Shapiro, N. M., and M. H. Ritzwoller (2002), Monte-Carlo inversion for a global shear velocity model of the crust and upper mantle, *Geophys. J. Int.*, *51*, 88–105.

Shapiro, N. M., and M. H. Ritzwoller (2004), Inferring surface heat flux distributions guided by a global seismic model:

Particular application to Antarctica, *Earth Planet. Sci. Lett.*, *223*, 213–224.

Shipboard Scientific Party (2004), Leg 209 summary, in *Proc. ODP, Init. Rep., 209*, edited by P. B. Kelemen et al., pp. 1–139, Ocean Drill. Program, College Station, Tex.

Smith, W. H. F., and D. T. Sandwell (1997), Global sea floor topography from satellite altimetry and ship depth soundings, *Science*, *277*, 1956–1962.

Stein, C., and S. Stein (2003), Mantle plumes: Heat flow near Iceland, *Astron. Geophys.*, *44*, 1.8–1.10.

Tanaka, A., Y. Okubo, and O. Matsubayashi (1999), Curie point depth based on spectrum analysis of the magnetic anomaly data in East and Southeast Asia, *Tectonophysics*, *306*, 461–470.

Tselentis, G.-A. (1991), An attempt to define Curie point depths in Greece from aeromagnetic and heat flow data, *Pure Appl. Geophys.*, *136*, 87–101.

Turcotte, D. L., and G. Schubert (2002), *Geodynamics*, 456 pp., Cambridge Univ. Press, Cambridge, U. K.

van Hunen, J., S. Zhong, N. M. Shapiro, and M. H. Ritzwoller (2005), New evidence for dislocation creep from 3-D geodynamic modeling the Pacific upper mantle structure, *Earth Planet. Sci., Lett.*, *238*, 146–155.

Vogt, P. R. (1991), Bermuda and Appalachian-Labrador rises: common non-hotspot processes?, *Geology*, *19*, 41–44.

Wang, T., J. Lin, B. Tucholke, and Y. J. Chen (2011), Crustal thickness anomalies in the North Atlantic Ocean basin from gravity analysis, *Geochem. Geophys. Geosyst.*, *12*, Q0AE02, doi:10.1029/2010GC003402.

Wasilewski, P. J., and M. A. Mayhew (1992), The Moho as a magnetic boundary revisited, *Geophys. Res. Lett.*, *19*(22), 2259–2262, doi:10.1029/92GL01997.

Wasilewski, P. J., H. H. Thomas, and M. A. Mayhew (1979), The Moho as a magnetic boundary, *Geophys. Res. Lett.*, *6*(7), 541–544, doi:10.1029/GL006i007p00541.

Wessel, P., and W. H. F. Smith (1995), New version of the Generic Mapping Tools (GMT) version 3.0 released, *Eos Trans. AGU*, *76*, 329.

Whittington, A. G., A. M. Hofmeister, and P. I. Nabelek (2009), Temperature-dependent thermal diffusivity of the Earth's crust and implications for magmatism, *Nature*, *458*, 319–321.

Yuen, D. A., and L. Fleitout (1985), Thinning of the lithosphere by small-scale convective destabilization, *Nature*, *313*, 125–128.